

# Deep HST Imaging of Sextans A I. The Spatially Resolved Recent Star Formation History

Robbie C. Dohm-Palmer

*Astronomy Department, University of Michigan, Ann Arbor, MI 48109*

rdpalmer@astro.lsa.umich.edu

Evan D. Skillman

*Astronomy Department, University of Minnesota, Minneapolis, MN 55455*

skillman@astro.umn.edu

Mario Mateo

*Astronomy Department, University of Michigan, Ann Arbor, MI 48109*

mateo@astro.lsa.umich.edu

Abi Saha and Andrew Dolphin

*National Optical Astronomy Observatories, 950 North Cherry Avenue, P.O. Box 26732, Tucson, AZ 85726*

saha@noao.edu, dolphin@noao.edu

Eline Tolstoy

*U.K. Gemini Support Group, Oxford University, Oxford OX1 3Rh, England*

etolstoy@astro.ox.ac.uk

Jay S. Gallagher

*Department of Astronomy, University of Wisconsin, Madison, WI 53706-1582*

jsg@astro.wisc.edu

and

Andrew A. Cole

*Astronomy Dept., 532 LGRT, University of Massachusetts, Amherst, MA 01003*

cole@condor.astro.umass.edu

**ABSTRACT**

We have measured stellar photometry from deep Cycle 7 Hubble Space Telescope/WFPC2 imaging of the dwarf irregular galaxy Sextans A. The imaging was taken in three filters: F555W ( $V$ ; 8 orbits), F814W ( $I$ ; 16 orbits), and F656N ( $H\alpha$ ; 1 orbit). Combining these data with Cycle 5 WFPC2 observations provides nearly complete coverage of the optically visible portion of the galaxy. The Cycle 7 observations are nearly 2 magnitudes more sensitive than the Cycle 5 observations, which provides unambiguous separation of the faint blue helium burning stars (BHeB stars) from contaminant populations. The depth of the photometry allows us to compare recent star formation histories recovered from both the main sequence (MS) stars and the BHeB stars for the last 300 Myr. The excellent agreement between these independent star formation rate (SFR) calculations is a resounding confirmation for the legitimacy of using the BHeB stars to calculate the recent SFR. Using the BHeB stars we have calculated the global star formation history over the past 700 Myr. The history calculated from the Cycle 7 data is remarkably identical to that calculated from the Cycle 5 data, implying that both halves of the galaxy formed stars in concert. We have also calculated the spatially resolved star formation history, combining the fields from the Cycle 5 and Cycle 7 data. The star forming regions are found in 3 major zones of the galaxy. One of these zones is extremely young, consisting of only a single star forming region which is less than 20 Myr old. Two of these zones are associated with high column density neutral gas, while the third, and oldest, is not. Our interpretation of this pattern of star formation is that it is an orderly stochastic process. Star formation begins on the edge of a gas structure, and progressively eats away at the cloud, breaking it up and inducing further star formation. A more quantitative analysis of the star formation process must await a larger sample of galaxies with spatially resolved star formation histories to allow correlation studies with the physical properties of the galaxy.

*Subject headings:* galaxies: evolution — galaxies: individual (Sextans A) — galaxies: irregular — galaxies: stellar content — stars: formation

## 1. Introduction

Dwarf galaxies are critical components in the evolution of the universe. High-redshift observations, and modern simulations of structure evolution within the framework of cold dark matter (Pearce et al. 1999; Steinmetz & Navarro 1999), suggest that large galaxies formed hierarchically through the progressive merger of smaller pre-galactic structures. Dwarf galaxies in the nearby universe are obvious candidates for the remains of these smaller objects (Tolstoy 1999). One significant problem with this interpretation is that models predict there should be far more dwarfs in the nearby universe than we observe (Klypin et al. 1999; Moore et al. 1999). Furthermore, the merger process clearly continues today, as evidenced by the Sgr dwarf (Ibata, Gilmore, & Irwin 1994), making the evolutionary role of nearby dwarfs ambiguous.

There are several puzzling aspects of nearby dwarfs that prevent us from clearly identifying their evolutionary role. Do nearby dwarfs represent the initial, intermediate, or final stages of hierarchical formation? Why did early-type dwarfs use up or lose all their gas, while late-types retain gas and continue to form stars? What is the relation between dI galaxies with low to moderate star formation rates, and more “bursty” galaxies with currently high star formation rates? Answers to these questions may depend critically on the merger history of the universe.

Resolved stellar populations in nearby galaxies can address many of these questions by directly determining the star formation history for these galaxies. However, in order to separate potential merger events from simple star formation events we must independently understand the star formation process. The physical motives for star formation in dwarf galaxies are very poorly understood. Unlike spiral galaxies (Roberts 1969; Kwan & Valdez 1987), dwarfs have no spiral density waves to mediate the formation of molecular clouds. This lack of global dynamic structure suggests that stochastic processes will play a significant, if not dominant, role in dwarfs.

If the star formation is stochastically induced, one might expect the history of a dwarf to be volatile: filled with large bursts of activity and lulls of inactivity. Certainly this characterizes the class of blue compact dwarf galaxies (Searle & Sargent 1972; Searle, Sargent, & Bagnuolo 1973). This type of behavior has also been demonstrated in several dwarf spheroidal galaxies whose color-magnitude diagrams (CMD’s) clearly show several major episodes of star formation with little activity in between (Smecker-Hane et al. 1994; Mighell & Rich 1996; Mateo 1998). However, the evolutionary role of these objects is ambiguous. Did these objects undergo this quasi-periodic behavior as a single entity, or as separate entities that have subsequently merged?

One might assume that dI galaxies undergo a similar history, and are the same type of galaxy as the more “bursty” objects, caught in a different phase of evolution. However, there is little evidence for pronounced starburst cycles among gas-rich field dwarfs in the present epoch (van Zee 2001; Gallagher, Littleton, & Matthews 1995). The lack of bursts in these isolated objects may be due to a lack of merger or interaction in their past. If so, these isolated dI galaxies may represent the most basic building block of larger objects. This is consistent with the recent observation that isolated objects closely match a closed-box chemical evolution model (Kennicutt & Skillman 2001).

In order to address these evolution processes we continue our study of star formation in the dI galaxy Sextans A. Our initial studies (Dohm-Palmer et al. 1997a,b) were based on a total of 2 orbits of WFPC2 images in the F555W and F814W filters. This field covered approximately half the visible portion of the galaxy. The current study adds Cycle 7 WFPC2 imaging in these same two filters totaling 24 orbits. This deeper field was approximately positioned to include the opposing half of the visible galaxy. In this paper we explore the spatially resolved star formation history of Sextans A. The next paper in this series will explore the intermediate to old ( $\geq 1$  Gyr) star formation history using the red-giant branch and red clump populations.

Our techniques for calculating the recent star formation history, discussed in detail in Dohm-Palmer et al. (1997b), utilize the Blue He-Burning (BHeB) supergiants to calculate both the

rate and location of star formation over the past 1 Gyr. This technique follows in the pioneering footsteps of the studies of the Large Magellanic Clouds by Payne-Gaposhkin (1973) and Isserstedt (1984). By combining these new Cycle 7 data with the previous Cycle 5 data, we obtain a nearly complete view of the visible galaxy. This allows us to make broader comparisons between local star formation properties and global properties. One appeal of resolved recent star formation histories is that it allows a detailed insight into the star formation process, allowing an investigation of the patterns of star formation and a comparison between the distributions of recently formed stars and the gas from which they formed (Isserstedt & Kohl 1984; Dohm-Palmer et al. 1998). Studies of many galaxies in this way will allow us to characterize properties such as typical duration of star forming episodes and typical sizes of star forming regions. They will also help us to better understand whether the star formation process is predominantly stochastic, or whether “triggers” are required.

More complete observational histories of Sextans A can be found in Dohm-Palmer et al. (1997a) and van den Bergh (2000). Since the study by Dohm-Palmer et al. (1997a), a detailed observational study has been conducted by Van Dyk, Puche, & Wong (1998). Van Dyk, Puche, & Wong (1998) measured *UBVRI* CCD stellar photometry using the KPNO 2.1m telescope and compared these to HI imaging and narrow-band H $\alpha$  imaging. They make extensive spatial comparisons of different age populations to conclude that star formation has been propagating outward from the center of the galaxy over the last 100 Myr. This is imminently relevant to our study, and we make detailed comparisons between their conclusions and ours in §5.3.

Arguably the most important parameter in calculating the star formation history from stellar populations is the distance (Tolstoy et al. 1998). We adopt the distance used in Dohm-Palmer et al. (1997a) of 1.44 Mpc ( $m - M_0 = 25.8 \pm 0.1$ ). This is a compromise between the cepheid determination and the RGB tip determination (Piotto, Capaccioli, & Pellegrini 1994; Sakai, Madore, & Freeman 1996). This is also the same distance adopted by Van Dyk, Puche, & Wong (1998).

In the following section we describe the new data set and image construction. This is followed by a discussion of the photometric measurement. The moderate stellar crowding in these deep images requires considerable care in modeling the PSF. We then compare the photometry with the Cycle 5 photometry for the small overlap region. Next, we describe the global star formation history calculation. We compare the results of using the main sequence to using the BHeB stars. We then use the BHeB stars to calculate the spatially resolved star formation history. The results of the spatially resolved history are compared with the conclusions of Van Dyk, Puche, & Wong (1998). A comparison is made with the neutral gas (HI) distribution. Finally, we discuss the implications for the star formation process and the evolutionary role of dI galaxies.

## 2. Observations and Image Construction

The images were taken with the Hubble Space Telescope (HST)/WFPC2 instrument between the dates of 5 April 1999 and 8 April 1999. Images in the F555W filter were obtained during 8 orbits, F814W during 16 orbits, and F656N during 1 orbit. Each orbit consists of two separate images, each 1200 seconds long. Thus, the total integration times were 19200 seconds in F555W, 38400 seconds in F814W, and 2400 seconds in F656N (Table 1). The images were taken in four different sub-pixel dithering positions. The orbits were divided evenly among the four positions. The images were calibrated in the standard HST pipeline reduction.

The first step is to combine the exposures into a single image for each filter. The images were shifted to align to the nearest integer pixel. To determine the shifts for each image, we used the DoPHOT program (described in more detail below) to measure the position of several thousand stars in each image. The stars from each image were matched and the coordinate transformation used to determine the nearest integer shift.

The images were then coadded, applying an anti-coincidence algorithm to detect and remove cosmic ray detections between pairs of images. The algorithm was optimized for the WFPC2 PSF and is described in Saha et al. (1996). All the images were combined in pairs, starting with the pairs taken in the same orbit, until a single image was obtained. At each combination cosmic ray detections were removed to only the 4-sigma level. While this potentially leaves some cosmic ray detections, this procedure is performed many times with successively less and less noisy images. Hence, the final images are quite clean of cosmic ray detections.

The final images are shown in Fig. 1. The HST images are overlaid on a ground-based image taken on the 0.9m at CTIO (Hunter 1997). We have also included the previous HST image of Sextans A, described in Dohm-Palmer et al. (1997a). We recreated the image for the old position to include only the F555W and F814W filters, so that it would match the colors of the new position. Where the Cycle 5 and Cycle 7 images overlap, the Cycle 7 image is shown.

The F656N image ( $H\alpha$ ) at the new position has been added in red. Note that the F656N image is much noisier than the other images (as expected for a narrow band image). The primary feature in the  $H\alpha$  is a large semi-circular shell. This was first seen by Hunter & Gallagher (1992), and later divided into 9 HII regions by Hodge, Kennicutt, & Strobel (1994).

## 3. Stellar Photometry

### 3.1. Photometric Measurements

Stellar photometry was measured from the final F555W and F814W images, following the procedure outlined by Dohm-Palmer et al. (1997a). The DoPHOT program (Schechter, Mateo, & Saha 1993) was used, with modifications for the under-sampled WFPC2 PSF, as described

in Saha et al. (1996). With the depth achieved in these images, there is a moderate amount of stellar crowding. DoPHOT attempts to overcome crowding difficulties by subtracting an analytic function from the image at the location of each identified star, thus isolating stars for photometric measurement.

In an uncrowded field, it is not important to precisely match the fitting function to the PSF. However, this is not the case in a crowded field. Residuals of the subtraction in neighboring stars can interact to mimic faint, noisy stars. This can change the photometric measurement by inadvertently removing flux from the image. This difficulty is further enhanced by the fact that the PSF in the WFPC2 images is under-sampled. Because the PSF covers few pixels, it is statistically easier for the interacting residuals to conspire to mimic faint stars. To avoid this problem as much as possible, we exerted great effort to match the analytic function to the PSF.

The shape of the fitting function in DoPHOT is controlled by 3 parameters:  $\beta_4$ ,  $\beta_6$ , and  $\beta_8$ . These parameters were determined following the method described in Dohm-Palmer et al. (1997a). In this method, the parameters are allowed to vary. For each parameter set, the function is fit to a group of bright stars, and subtracted from the image. The parameter set that leaves the smallest residual is chosen as the best. We found that the best overall results were achieved by using the same set of  $\beta$  values for all WF chips and a different set for the PC, while letting the FWHM vary from chip to chip. The values used for this data set are given in Table 2.

Despite the effort, the fitting function does not match the PSF perfectly, and there is still a need for an aperture correction. The aperture corrections were measured with an aperture of  $0.5''$  around the brightest stars with internal DoPHOT errors less than 0.04. A polynomial, quadratic in position, was fit to these values. Table 3 lists the aperture correction fits for each chip and filter. Also listed are the number of stars used in the fit, and the RMS residual of the fit.

The first thing to notice is that the quadratic fits were only slightly better than fitting a constant value. This is reflected in the small coefficients. Second, the correction is quite small. To demonstrate this, the aperture corrections for the center of each chip are also listed in Table 3. The central value is less than the RMS residual of the fit in all but one case. This indicates we likely could not improve the choice of  $\beta$  parameters without letting them vary spatially across each chip.

### 3.2. Photometric Results

Once the stellar photometry was obtained from the final F555W and F814W images, the two lists were matched to within a radius of 0.5 pixels. Prior to calibration, the photometry was corrected for charge transfer efficiency (CTE) using the equations of Whitmore, Heyer, & Casertano (1999), which have been verified by the study of Dolphin (2000). We used the transformation to  $V$  and  $I$  in Holtzman et al. (1995).

We adopted the Galactic reddening value of  $E(B - V) = 0.043$  and the extinction coefficients

given in Schlegel, Finkbeiner, & Davis (1998):  $A_V = 3.315E(B - V)$  and  $A_I = 1.940E(B - V)$ . This gave  $A_V = 0.143$  and  $A_I = 0.083$ . These extinction values are slightly higher than was used in Dohm-Palmer et al. (1997a), however the difference in  $E(V - I)$  is only 0.01. The low values of extinction are consistent with the high Galactic latitude of Sextans A ( $+40^\circ$ ) and the low metal abundance of its ISM (Skillman, Kennicutt, & Hodge 1989). This low overall extinction is probably critical in the clear separation of the bright MS and BHeB stars. The low extinction puts a strong upper limit on the degree of differential reddening that can broaden the two bright blue star features. The importance of this effect has been clearly demonstrated for the Large Magellanic Cloud (Harris, Zaritsky, & Thompson 1997; Zaritsky 1999).

The internal DoPHOT measurement errors are shown in Fig. 2. The  $V$  data are slightly deeper than the  $I$  data. The present data are deeper than the Cycle 5 data by 1.5 mag and 1.8 mag in  $V$  and  $I$  respectively. Most of the points follow the standard pattern of broadening and increasing toward fainter magnitude. The scatter of points above this curve comprise about 4% of the data. This is a slightly higher fraction than was observed in the Cycle 5 data, which we attribute to the effects of crowding.

We performed artificial star tests, following the procedure detailed in Dohm-Palmer et al. (1997a). The PSF was created by averaging between 10 and 20 stars for each of the WF chips, and 4 stars for each of the PC chips. While this is a small number of stars for the PC, we preferred to accept only bright, completely isolated stars. The high stellar density limited the availability of such stars. The broadening factor due to the under-sampling of the PSF (see Dohm-Palmer et al. (1997a)) was measured to be  $\sim 1.1$ , and varied from chip to chip by 4%.

Artificial stars were added to 100 copies of the final images in both filters. Each copy contained artificial stars numbering 2% of the detected real stars. The artificial stars were distributed with a power law of slope 0.35 in  $V$ , matching the real data, and a uniform color distribution with  $-1 < V - I < 2$ . DoPHOT was run on each frame identically to the original images. The data were then matched and calibrated identically, including the CTE correction. Finally, the star lists were matched with the lists of artificial stars.

The results of the artificial star tests are shown in Fig. 3 as plots of incompleteness versus magnitude. Errors in the histogram are from Poisson statistics based on the number of input artificial stars. As described in Dohm-Palmer et al. (1997a) the faint end of the completeness curves needed to be corrected for Malmquist bias. Also, the bright end was fairly noisy, producing undesirable structure. To avoid introducing this structure to the later calculations we have boxcar smoothed the curves brighter than 25 magnitudes.

Notice that for magnitudes between 22 and 26 nearly 20% of the artificial stars are missing. This is an effect of the high stellar density. These stars have been blended with existing stars, and thus were removed from the detection list. Despite the crowding, the photometric fidelity of the detected, non-blended, artificial stars was excellent. The recovered magnitudes agreed with the input magnitudes consistent with the random noise.

### 3.3. Comparison to Cycle 5 Photometry

There is a small region of overlap between the Cycle 5 and Cycle 7 data sets. We have compared the photometry for stars in this region as a check on the photometric consistency. Approximately 8200 stars were found in common in this region. There is a small zero-point offset between the two data sets ( $\sim 0.03$  mag). In both cases the offset is such that the Cycle 7 data are brighter. Since the offset is nearly the same in both  $V$  and  $I$ , the color index  $V - I$  is practically identical for the two data sets. We believe this small offset is due to the CTE correction, which has a large time dependence. Whitmore, Heyer, & Casertano (1999) suggest the correction is only good to  $\sim 5\%$ . In this case the agreement is good to  $\sim 3\%$ , which is probably as good as can be expected.

The CMD's for Cycle 7 and Cycle 5 are shown in Fig. 4. Also plotted in each are curves indicating the main sequence (MS), the blue edge of the He-burning loop (BHeB), and the red edge of the HE-burning loop (RHeB). These curves come from the stellar evolution models of Bertelli et al. (1994). Notice the excellent agreement between the models and the observations. In particular, the faint end of the BHeB sequence is now very well detected, and follows the model prediction with exquisite accuracy. Brighter than  $V = 22$  the model prediction and observations diverge slightly. This corresponds to a stellar mass of about  $5_{\odot}$  and an age of about 100 Myr.

The most obvious difference between the two data sets is the fainter limits of the Cycle 7 data. The main sequence is fully 2 magnitudes deeper. Furthermore, the faint limit of the red clump has clearly been detected, while only the bright end was detected by the Cycle 5 data. The bright portion of the CMD's are remarkably similar. The MS, BHeB and RHeB stars all appear in the same positions with similar densities. In particular, the increased density of BHeB stars near  $V \sim 24$  is present in both data sets. The increased quality of the the Cycle 7 data shows this to be a clear density enhancement. We shall discuss the implications of this feature in the next section.

## 4. Recent Global Star Formation History

In the following sections we calculate the recent star formation history (SFH) based on the MS and BHeB populations. To separate these populations, selection polygons were created. The polygons are based on the  $Z = 0.001$  model curves of Bertelli et al. (1994) (Fig. 4). The average color index error was used to determine the width of the polygons as a function of magnitude. Because the observed BHeB sequence does not follow the model for  $V < 22$  a constant color cutoff of  $V - I = -0.1$  was used instead. The selection polygons are shown in Fig. 4.

Also indicated in Fig. 4 is a selection region for the red giant branch (RGB). We did not include the red clump stars in this selection in order to obtain the oldest possible star sample. There are some younger evolutionary phases that may be included, such as the asymptotic giant branch. However, the RGB region should be dominated by stars older than 2 Gyr. These stars are not used in this paper for numerical calculations, so the selection polygon was chosen by hand.



However, care was used to ensure that none of the polygonal regions overlapped.

#### 4.1. Main Sequence Stars

The luminosity function for the main sequence is shown in Fig. 5. The error bars represent Poisson errors. The turnoff age is indicated for several locations. There are some subtle changes in slope near  $V = 22$ , and  $V = 24$ . Other than this, there are no discernible features. Fig. 5 also shows the MS luminosity function for the Cycle 5 data as a dotted line. The same selection region in the CMD was used to isolate the MS in both the Cycle 7 data and the Cycle 5 data. Other than the photometric depth, the two histograms are very similar.

Following the prescription of Dohm-Palmer et al. (1997a) we have calculated the cumulative mass of stars formed based on the main sequence luminosity function, and then calculated the star formation rate (SFR) from the slope of this curve. The result is shown in Fig. 6. We calculated the SFH using two different sets of models to demonstrate the dependence of the calculation on the model uncertainties. The left panel shows the calculation using the Padua,  $Z = 0.001$ , stellar isochrones of Bertelli et al. (1994). The right panel shows the calculation using the Geneva,  $Z = 0.001$ , stellar evolution models of Schaller et al. (1992). In both cases we assumed a power law IMF with a Salpeter (1955) slope ( $-1.35$ ) normalized as described in Dohm-Palmer et al. (1997a). We also normalized all values by the field of view of the WFPC2 instrument. For the adopted distance modulus (25.8) this is an area of  $0.90 \text{ kpc}^2$ . Note that the bins are constant width in magnitude, and thus vary in width with age. The error bars represent Poisson errors based on the total number of stars in each bin and do not include terms to account for the uncertainties in the stellar evolution models.

The main feature of the Padua SFH is a strong peak near 25 Myr. The slope change in the luminosity function near  $V = 22$  is the rise to this peak, while the slope change near  $V = 24$  is the sharp drop-off at 30 Myr. Older than this there is a nearly constant value, 3-4 times lower than the peak. There is some variation from bin to bin for these older times, but none of the structure is very significant within the statistical noise. For the youngest bins ( $< 25 \text{ Myr}$ ), the sparsity of stars leads to a highly uncertain value, but the star formation rate generally decreases toward the youngest ages.

The Geneva calculation has the same general form, but the peak is shifted to near 50 Myr and is not as large in value. However, the ratio of the peak value (near 25 Myr in the Padua case, and near 50 Myr in the Geneva case) to the off peak values (older than 50 Myr in the Padua case, and older than 75 Myr in the Geneva case) is the same for both models. In other words, both models predict a rise in the SFR in recent times by the same factor. The models disagree in the exact age of the rise and the actual values of the SFR. The reason for the disagreement is because the Geneva models predict a slightly lower mass star, and a slightly older turnoff age, for a given magnitude. Because of the lower mass, the IMF correction is smaller, hence the SFR is smaller. Thus, the

calculations are demonstrating the same behavior, there is just disagreement (of order a factor of two) between the models on the exact normalization values.

Finally, we note that part of the uncertainty in the MS calculation is endemic to this phase of evolution. Any given location along the MS can have stars of any age younger than the turnoff age. However, the situation is even more complicated. The MS stars evolve in luminosity during the MS phase. Thus, any given magnitude can have stars of differing mass that may or may not have the same age. Thus, there is an inherent age and mass resolution limitation on the MS. Because of this, the MS is not well suited to this type of analysis, where we calculate the SFH directly from the luminosity function. The MS can be modeled more accurately with Monte Carlo modeling. The calculation performed here is primarily for a consistency check on the BHeB calculation, which we discuss in the next section.

#### 4.2. Blue He-Burning Stars

The luminosity function for the BHeB stars is shown in Fig. 7. The error bars are calculated as in Fig. 5. The most striking feature is a plateau between  $V = 21$  and  $V = 22.5$ . A flattening indicates a reduction in the SFR. Other than this, the luminosity function is fairly featureless, except for a few bumps that are not very statistically significant.

For comparison, we have also plotted the BHeB star luminosity function for the area of the galaxy covered in the Cycle 5 observations. We used the same selection region in the CMD for the Cycle 5 data as we did for the Cycle 7 data. For calculating the SFR from the BHeB stars, it is not the slope of the luminosity function which is important, but the actual number count in each bin. The slope indicates the derivative of the star formation rate with time. The Cycle 5 and Cycle 7 data do show some differences in slope at various locations, but, overall, the counts are similar for  $V < 24$ . For fainter magnitudes, the Cycle 5 data show an excess of stars compared to the Cycle 7 data. This is because of contamination by MS and red clump stars, which have scattered into the selection region through photometric errors (see Fig. 4). Note that the Cycle 5 luminosity function could be smoother because of the larger photometric errors at a given luminosity.

From the BHeB luminosity function we have calculated the SFR back to 700 Myr (Fig. 8). The calculation normalizes the star count in each bin for the IMF, and the length of time stars spend in the BHeB phase. The details of the calculation can be found in Dohm-Palmer et al. (1997a). We used the  $Z = 0.001$  stellar evolution models of Bertelli et al. (1994), and a power law IMF with a Salpeter (1955) slope ( $-1.35$ ). Because of model uncertainties in the BHeB phase of very massive stars ( $> 15 M_{\odot}$ ), we restrict the calculation to lower masses, and hence ages older than 20 Myr. We treated the BHeB identically to the MS stars in that we normalized all values by the field of view. Again, the bins are constant width in magnitude, and thus vary in width with age.

Since the BHeB sequence does change in temperature, with redder colors at decreasing luminosity, we were concerned that simply binning the star counts as a function of luminosity might

introduce a bias. We experimented with a method to account for this. Instead of simply normalizing a star based on its magnitude, we also used the color index to normalize by the properties of the closest point on the BHeB model curve in the CMD. We found this made no difference in the SFR calculation. The reason is that the dynamic range of the BHeB sequence in color index is much smaller than it is in magnitude, with the result that accounting for the color index changed the normalization values very little.

As we saw with the MS (Fig. 6), the main feature of the SFH is a peak near 25 Myr. As in the MS SFH, there is an abrupt drop-off at 30 Myr, and then the SFR decreases with older times, until leveling out near 100 Myr. Older than 100 Myr the SFR is constant within the statistical noise, at a level that is roughly 9 times lower than the peak value. The peak value actually depends somewhat on the choice of bin size. The actual duration of the star formation event compared to the bin size is the determining factor. If the bin size is smaller than the star forming duration, the event is divided among several bins. If the bin size is larger than the duration, the peak is smoothed. We have chosen a bin size (0.3 magnitudes) that gives a peak near maximum value. Because the calculation was restricted to ages older than 20 Myr, there is no evidence of the decrease in SFR at the youngest ages.

Fig. 8 also shows the SFH calculation based on the other half of the galaxy covered in the Cycle 5 data. It is striking that for ages younger than 300 Myr, the two curves are nearly identical in form and value. This need not have been the case since the two data sets cover different portions of the galaxy. This indicates that, globally, the galaxy seems to have followed the same history throughout the entire optical body. For ages older than 300 Myr, the Cycle 5 data indicates a higher SFR than the Cycle 7 data. As discussed above, this excess is likely due to contamination by MS stars and red clump stars scattering into the selection region.

Finally, we have plotted the SFH based on the Cycle 7 BHeB data alongside the SFH based on the MS (Fig. 6) using both the Padua and Geneva models. In this case we are hoping for agreement because it is the SFH of the same region of the galaxy calculated in two different, and independent, ways. The Padua models show excellent agreement in form and value between the MS and BHeB stars. Specifically, both methods exhibit a strong peak at 25 Myr, with nearly the same value. The sharpness of the drop-off at older ages also appears in both datasets, with the depth of the drop-off statistically identical. For older ages ( $> 30$  Myr), both methods exhibit a nearly constant, and lower, SFR. The one notable difference is that for times older than 100 Myr, the BHeB calculation is consistently lower than the MS calculation by roughly a factor of two.

The Geneva model’s BHeB calculation does not agree quite as well with the Geneva MS calculation for the youngest ages. As discussed in Sec. 4.1, the Geneva MS SFH is shifted to older ages by roughly 25 Myr, and the SFR values are lower, compared to the Padua MS SFH. However, the MS and BHeB calculations for ages older than 75 Myr agree better in the Geneva models than they do in the Padua models. These differences represent systematic model uncertainties in the SFH calculation, as well as inherent difficulties in using the MS for this type of analysis (see Sec.

4.1).

Notice that the BHeB calculations of both models (dotted lines in Fig. 6) agree with one another extremely well in both age and value. This indicates the relevant model parameters for the BHeB evolutionary phase are nearly identical in both models. The BHeB phase is also not nearly as limited by mass and age resolution as the MS, which contributes to this agreement. Thus, for this type of analysis, where the SFR is calculated directly from the luminosity function, the BHeB stars prove more reliable than the MS.

The excellent agreement between the independent SFR calculations in the shape and amplitudes of most of the SFR values is a resounding confirmation for the legitimacy of the using the BHeB stars to calculate the SFR. The MS is certainly the best understood of the phases of stellar evolution, and tying results of the BHeB stars to those of the MS provides the strongest test of this method. Due to brightness limitations, for most galaxies we will not be able to produce recent star formation histories from MS stars, but the BHeB stars allow us to study the recent star formation histories of galaxies beyond the Local Group!

## 5. Spatially Resolved Studies of Sextans A

### 5.1. Spatial Distributions of Stellar Populations

A first cut at a spatially resolved star formation history is to divide the CMD into broad groups, such as the MS, BHeB, and RGB. When discussing the spatial density of stars, it makes sense to include both the Cycle 5 and Cycle 7 data to obtain a nearly complete view of the optical galaxy. In order to orient the reader to these composite density plots, we include Fig. 9. This is a reproduction of the HST portion of Fig. 1 rotated so the edges are parallel with the plot axes. The Cycle 5 image is in the lower left with the PC toward the upper right. The Cycle 7 image is in the upper right rotated  $\sim 180$  degrees relative to the Cycle 5 image.

Fig. 10 shows the stellar density for the current positions of the MS and BHeB stars divided into four different age groups. The density maps were made by placing the stars in a spatial grid, and convolving the grid with a Gaussian kernel. We used  $\sigma = 80$  pc for the Gaussian width. For reference, one star per convolution beam is 25 stars  $\text{kpc}^{-2}$ . We divided the luminosity functions into 4 age groups. One must keep in mind that, for the MS, these groups contain stars for all ages younger than the labeled age limits. This is not true of the BHeB stars whose ages are restricted to within the stated age limits. In both cases, these maps have not been normalized for IMF, so the numerical values are not directly comparable between different age groups.

Starting with the upper left hand panel in Fig. 10, the youngest MS stars are very concentrated in 3 locations that are about 5 times as dense as the intervening space. These high density concentrations are the sites of the most recent star formation activity. They are apparent in the image (Fig. 9) as locations of bright blue stars, and  $\text{H}\alpha$  emission. These same concentrations appear in

the next oldest category (50-100 Myr) as well. This is not necessarily because these star forming regions existed between 50 and 100 Myr ago. Rather, it is because different age populations overlap along the main sequence such that selecting stars by the turnoff age includes some stars from all younger generations as well.

If one accounts for the contamination of younger generations, we see clear differences between the youngest main sequence density map and the next older one (50-100 Myr). The highest density regions are now located in different places. For example, in the upper left portion of the figure, the density peak has shifted from  $x \sim 450$ ,  $y \sim 1375$  to  $x \sim 200$ ,  $y \sim 1125$ . From this we infer that the sites of star formation have changed over this 50 Myr time scale.

In the oldest two MS star groups, the most obvious change is the lack of stars in the Cycle 5 portion of the diagram. This simply reflects the brighter photometric limits of that data set. In the Cycle 7 portions of the plots, the stars still concentrate, but not as strongly as in the younger groups. The contrast between the peaks and intervening space is roughly a factor of 2. Our interpretation is that the concentrations are stars which are younger than the turnoff limits we used, and are associated with the youngest groups. The older stars, present because of the older turnoff limits, are not so concentrated. The lower contrast can be attributable to either lower star formation rates or the possibility that these older stars have had time to disperse from their formation sites.

We now focus on the BHeB stars in the lower panels of Fig. 10 for comparison. Since the BHeB selection does not mix ages, they provide a better picture of how the star formation actually has changed in this galaxy. In the youngest group, the BHeB stars are highly concentrated, just as they were for the MS. As expected, two of the concentrations coincide with two of the MS concentrations. The third MS concentration in the youngest group (towards the upper right) is not present. Since we have restricted the BHeB stars to only those older than 20 Myr, we infer that this third region is younger than 20 Myr. Note also that the peak locations in the BHeB stars do not exactly match up with the peaks in the MS stars. These small differences are probably due to the 20 Myr restriction on the BHeB stars. This indicates that the sites of star formation concentrations can migrate noticeably on time scales as short as 10 Myr.

The differences between the youngest group and the 50-100 Myr group is quite dramatic. Two strong concentrations, especially the one near  $x = 250$ ,  $y = 850$ , appear without any indication in the younger group. Furthermore, these prominent concentrations are not present in the next oldest group (100-150 Myr). This is another indication that in some cases the timescale for change is much less than 50 Myr.

The oldest two groups still contain concentrations of BHeB stars, but at much lower contrast to the background, and much lower signal-to-noise ratio. This may reflect the overall lower SFR, as well as the diffusion of star forming regions over time. The appearance of these concentrations implies that the BHeB stars of this age do retain at least some spatial structure from their formation, even if they have begun dispersing. That is, if there were no concentrations at these older ages, it would imply that the timescale for the dispersion of star forming regions is less than roughly

100 Myr. We may infer that this timescale is longer than 100 Myr, but the effect is not strongly constrained by these data due to the low number counts. Ideally, one would like to observe a number of star formation sites of different ages, in order to compare the linear sizes as a function of time. Since there are no galaxies that provide high absolute SFRs over sufficiently long periods of time ( $\approx 1$  Gyr), this type of study will need to be conducted by comparing similar observations of many different galaxies.

It is interesting to note that there is a lack of BHeB stars in the upper right portions of the density maps. The extreme upper right corner is beyond the edge of the optical portion of the galaxy. But even within this edge there are fewer BHeB stars than on the other side of the galaxy. It is apparent that over the last 200 Myr this part of the galaxy has been relatively quiescent. It is only in the last 20 Myr that we see signs of activity, from the MS.

Finally, we can compare the density of the youngest stars with the oldest stars in the CMD, namely the RGB. The density of these older stars is shown in Fig. 11. They have not been divided into age groups, as this is a difficult task beyond the scope of this paper. The most marked difference between these older stars and the youngest stars is the lack of clumping. Being older, these stars have had plenty of time to migrate from their birthplace, and distribute themselves within the galactic potential. The RGB stars are centrally concentrated, with a strong bar feature through the center of the galaxy. We measure the position angle of this feature to be  $49^\circ \pm 2^\circ$ . This matches the major axis of the HI distribution (Skillman et al. 1988). Furthermore, Skillman et al. (1988) perform a dynamical analysis with a bar potential, and find the projected morphological axis of the bar to be  $52 \pm 3^\circ$ , matching well the observed stellar bar.

It is interesting to note that the distribution of the red clump stars do not follow this bar structure. The red clump contains stars as young as 1-2 Gyr. Although we have not yet determined an age distribution for these stars (to appear in a future paper), we assume that most of these stars must be younger than the RGB to mask the bar signature. From this we can infer that it must take at least this long for stars to relax into the barred potential. It is also interesting to note that the current star formation does not take place along the bar. In fact, the highest density HI regions, where stars are currently forming, are nearly perpendicular to the bar.

## 5.2. The Spatially Resolved Star Formation History

Following the methods of Dohm-Palmer et al. (1997b) we have created two movies showing the SFR, as determined by the density of BHeB stars, as a function of position and time. The first movie ranges from 20 Myr to 700 Myr in 10 Myr steps. The images have been convolved with an ellipsoidal Gaussian kernel with  $\sigma_{xy} = 80$  pc and  $\sigma_t = 30$  Myr. Still images from the movie are shown in Fig. 12. The movie includes both the Cycle 5 and Cycle 7 data, and has orientation the same as Fig. 9.

By 500 Myr the contrast between the peaks and intervening space is not as large as in younger

ages. There are two reasons for this. First, for these oldest times, there is some photometric contamination from other populations, such as the red clump. This is particularly true of the Cycle 5 (lower left) part of the image, where the photometric depth does not unambiguously separate the faintest BHeB stars from other populations.

A second reason for the smaller contrast may be dynamical. Based on the density plots above (Fig. 10) we concluded that the dynamical timescale for dissolution of a star forming region is at least 100 Myr, but this number must also have an upper bound, given the smoothness of the old star distribution. Thus, by 500 Myr, the star forming regions, while still detectable, are likely to be less concentrated. A comparative discussion of the theoretical work relevant to this question is given in the appendix of Dohm-Palmer et al. (1997b).

The linear time resolution is much shorter for the youngest stars than it is for the older stars. In order to take advantage of this we have made a second movie ranging from 20 Myr to 100 Myr in 2 Myr time steps. This movie was also convolved with  $\sigma_{xy} = 80$  pc, but  $\sigma_t = 6$  Myr. Still images from this movie are shown in Fig. 13.

The first thing to notice about the younger ages is the difference in transfer function. The SFR ranges from 0 to  $15000 M_{\odot} \text{ Myr}^{-1} \text{ kpc}^{-2}$  as opposed to 0 to 4000 for the older movie. This emphasizes what is apparent in the global SFH (Fig. 8), which is that the SFR jumps dramatically in the last 100 Myr. Another feature to notice is that the contrast between the star forming regions and intervening regions is much higher than for older times. The primary reason for this is the higher SFR, which naturally creates a higher contrast. Furthermore, these regions are very young and have not yet begun to disperse from their birthplace.

Finally, we wish to point out that there is no *concentrated* star formation in the upper right part of the image until the most recent times ( $< 40$  Myr). It is only in the last 20 Myr that that this part of the galaxy starts to form stars with comparable vigor. The star formation associated with the strong H $\alpha$  emission in the upper right (western) side of the galaxy is clearly very young. This is somewhat surprising since it is associated with one of the highest column density gas regions in the galaxy.

By contrast, the prominent group of blue stars in the lower left (eastern) part of the galaxy has been forming stars for at least 200 Myr. This activity is associated with the highest column density gas region in the galaxy. The peak location of the activity shifts around, but always remains near this high density gas cloud. There are also several lulls in the activity during this 200 Myr time span. So it appears that this region has been active during several different episodes over this time period. This is similar to the pattern of star formation seen in GR8 by Dohm-Palmer et al. (1998).

### 5.3. Comparison With Van Dyk et al. (1998)

Van Dyk, Puche, & Wong (1998) performed a comprehensive study of the stellar population

and ISM of Sextans A. Their major conclusion is that an increase in star formation activity began approximately 50 Myr ago in the center of the galaxy and progressed outward such that the most recent activity is taking place on the inner edge of the HI ring. This model implies that the star formation is taking place in discrete regions, rather than uniformly distributed throughout the galaxy. They interpret this to mean that the central activity created a supernova driven hot bubble which expanded outward. As the bubble expanded it compressed the gas and sequentially induced star formation.

A comparison between the location of the youngest MS and BHeB populations is quite favorable. Comparing their Fig. 6 with our Fig. 10 shows strong concentrations of both MS and BHeB stars in the northern and eastern corners of the optical galaxy. Also apparent are some BHeB stars in the center of the galaxy. Finally, the youngest star forming region in the western corner of the galaxy shows a strong concentration of young MS stars, but almost no BHeB stars. Because of the lack of BHeB stars in this western region, Van Dyk, Puche, & Wong (1998) also conclude this is one of the youngest regions of the galaxy, possibly as young as 15 Myr.

We also find that the central region of the galaxy was more active 50 Myr ago than it is today. However, the amplitude of the 50 Myr old central star formation event is not impressive, nor do we see an age progression from the center outward. In support of their model, Van Dyk, Puche, & Wong (1998) highlight the lack of young stars in the center of the galaxy. The youngest stars are, instead, found along the inner edge of the HI ring, and our observations show this as well. However, the converse is not true. We do not find a lack of older stars along the inner ring of HI. In particular, the 50 Myr frame of Fig. 13 clearly shows that while the central regions were forming stars, so were the northern (upper left) and eastern (upper right) portions of the inner ring edge, at the same rate or higher. The lack of older stars on the inner edge of the HI ring in the data of Van Dyk, Puche, & Wong (1998) may be due to the poorer spatial resolution afforded by their ground based data. At lower resolution, the brightest stars of a young population can completely hide an underlying older (fainter) stellar population.

Thus, our observations do not support the conclusion that the recent increase in SFR started in the center and progressed outward. Rather, it seems to have started in localized regions throughout the galaxy, but confined to the regions inside the HI ring. This argues that the HI ring probably existed prior to 50 Myr ago (which is supported by our observation of enhanced star formation in the vicinity of the present day HI concentrations hundreds of Myr ago). We cannot rule out the possibility that the star formation in the center of the galaxy 50 Myr ago cleared away gas which led to enhanced star formation in the outer parts. We can only conclude that this was not the dominant process involved in the recent star formation history of Sextans A. Since there is currently a lack of neutral gas in the central region, it could have been used up by the star formation activity 50 Myr ago, been heated by this activity, or the “hole” could have pre-existed this activity.



#### 5.4. Neutral Gas Comparison

We have obtained Sextans A 21-cm spectral data from the Very Large Array (VLA) <sup>1</sup> archive to create maps of the neutral gas. The data consisted of C-array data obtained in May 1992, and D-array data obtained in July 1992. Since these observations are used only to show the relationship between the star forming regions in the current study and the HI distribution and they are in good agreement with previously published HI observations (Skillman et al. 1988; Van Dyk, Puche, & Wong 1998), we only briefly outline their creation below.

All processing steps were performed with standard VLA reduction software in the NRAO AIPS environment. The two data sets were first calibrated, then combined. The continuum was determined from line free channels, and subtracted in UV space. The channel maps were constructed with the AIPS task IMAGR, using the default (“robust”) weighting scheme. This aided in optimizing the trade-off between signal-to-noise ratio and angular resolution when combining the data from the two different array configurations. A process called conditional transfer was used on the channel maps to remove noise spikes. Finally, the flux was converted into gas column density (Giovanelli & Haynes 1988).

The HST images were created from the final, coadded, F555W images, as described in Sec. 2. All four chips were combined into a single image using the IRAF/STSDAS<sup>2</sup> routine wmosaic. The equatorial coordinates of the HST images were needed to accurately overlay HI contours. These were determined using stars from the USNO-A2 catalog (Monet et al. 1998). Both the Cycle 5 and Cycle 7 images each had only a dozen stars available for this transformation. Because of the low number of stars, only a shift and rotate solution was determined, rather than a full distortion map. The solution was found interactively using the IRAF/FINDER package.

The HST images with HI contours are shown in Fig. 14. The gas has two kidney-shaped high density structures on opposite sides of the galaxy, connected by a lower density ring. The optical portion of the galaxy is coincident with the central HI depression. The most recent star formation, including the concentration that is younger than 20 Myr towards the northwest, lies near the inner edge of the highest density HI. The fact that the star formation is associated with the HI is not surprising and has been noted elsewhere (Skillman et al. 1988; van Zee et al. 1997; Van Dyk, Puche, & Wong 1998). What is not so obvious from Fig. 14, and may be seen more clearly in Fig. 12 of Van Dyk, Puche, & Wong (1998) is that for the SE HI concentration, the recent star formation overlaps with highest column density peak, while for the western HI concentration, the star formation appears to be confined to the inner edge. It is also interesting to note that the HI column density is relatively high across the entire optical disk of the galaxy; that is, the HI column

---

<sup>1</sup>The VLA is a telescope of the National Radio Astronomy Observatory which is operated by Associated Universities, Inc., under a cooperative agreement with the National Science Foundation.

<sup>2</sup>IRAF is distributed by the National Optical Astronomy Observatories, which are operated by the Association of Universities for Research in Astronomy, Inc., under cooperative agreement with the National Science Foundation.

density never drops below  $10^{20}$  atoms  $\text{cm}^{-2}$ . Thus, it is probably misleading to refer to a central “hole” in the HI distribution, and more apt to label that feature as a depression. However, the density of this depression is nearly an order of magnitude below the nominal critical density for star formation ( $10^{21}$  atoms  $\text{cm}^{-2}$ ), as discussed in Skillman, Kennicutt, & Hodge (1989). Note that the recent star formation in the SW corner of the galaxy is associated with an HI column density which is comparable to that found in the central depression.

## 6. Discussion

When discussing the spatial structure of a galaxy, one must ask how long the features which define a structure will survive, and how their overall spatial pattern may change with time. A complete discussion of this for Sextans A can be found in the appendix of Dohm-Palmer et al. (1997b). One of the most important points to remember for Sextans A is that the galaxy is rotating in nearly solid body rotation. Thus, there is no shear to break apart structures, or to separate gas from stars, although such separation can occur through other means such as supernova or wind-driven shocks.

There are three major associations of star formation visible in our field of view over the past 500 Myr. The oldest is the northern (upper right) portion of the galaxy. This coincides with an apparent gap between the two primary HI structures. Stars have been forming in this region of the galaxy for at least 400 Myr, or longer. The central location of the star formation does not remain fixed, but migrates around within this region. The relative lack of gas in this region would indicate that star formation can not be much longer sustained.

The second oldest region is in the east-southeast portion of the galaxy. This is associated with the highest column density gas. This region has been forming stars for at least 200 Myr. Again, the central location seems to migrate around within this region.

Finally, the youngest region in the west-northwestern portion of the galaxy is younger than 20 Myr. There has been no star formation in this region over the past 700 Myr despite the current presence of the second highest column density gas structure.

This pattern of star formation leads us to the scenario of an orderly stochastic process. We envision the star formation as burning through the gas clouds like a lit fuse. The star formation is induced on the edge of a cloud. The resulting supernova and wind-driven shocks break apart the clouds and induce further star formation, progressively eating their way through the gas structure.

It remains unclear what induced the rise in SFR over the past 50 Myr. However, given the stochastic nature of the star formation in these small irregular systems, it may be that this is simply a positive fluctuation within the expected variation. In fact, it may be that the galaxy has gone through similar fluctuations in the past 700 Myr, but they are smoothed by limitations in our time resolution.

It is also remarkable that both halves of the galaxy have undergone the same spatially averaged history, since the local behavior appears quite different. Even though the localized star forming regions are stochastic in nature, it appears that there is some global regulatory process that controls the average SFR. Sextans A is a member of a group of four galaxies (with Sextans B, NGC 3109, and the Antlia dwarf) which are probably bound and lie just outside of the zero-velocity surface of the Local Group (van den Bergh 2000). With very similar radial velocities and a separation of only 280 kpc, it is possible that Sextans A and Sextans B represent a bound pair. Thus, it is also possible that the orbital histories of these galaxies provide a major influence on their star formation histories. Another possibility is that the barred potential can play some regulatory role, similar to spiral arms in larger galaxies.

### 6.1. Star Formation Models and Future Analysis

We are reluctant to over-interpret the observations of Sextans A alone for two reasons. First, Sextans A may be in an unusual state compared to other dI galaxies. For example, Sextans A has a color index of  $B - V = 0.26$  (Hunter & Plummer 1996) which is much redder than the typical isolated dI, which has a median value of  $B - V = -0.22$  (van Zee 2000). In addition, the large superbubble structure seen in the HII distribution is unusual for dI galaxies, which typically have centrally concentrated HII complexes (Roye & Hunter 2000). It is possible that Sextans A is going through a rare increase in activity. Such fluctuations may occur in most, if not all, dI galaxies, but do so infrequently so that they are not seen in many galaxies. These events could easily be hidden in the past by the limitations of our time resolution in determining SFH's.

Second, one would like to observe a large number of star formation events over time to obtain a coherent picture of the regulatory processes of star formation. Unfortunately, the size of the galaxy, and the limited look-back age, allow us only to observe a few such events, which is not statistically significant. Since there are no galaxies that provide high absolute SFRs over sufficiently long periods of time ( $\approx 1$  Gyr), this type of study will need to be conducted with similar observations of many different galaxies. This will allow a comparative analysis to look for physical characteristics in the star formation process that are common to all dI galaxies. Several excellent comparative studies have been done using  $H\alpha$  observations (Hunter, Elmegreen, & Baker 1998; Elmegreen & Hunter 2000). However, these studies provide only a snapshot of the most recent (a few Myr) activity. This does not allow one to see how a star forming region changes with time, and link such changes to physical characteristics of the host galaxy.

Until spatially resolved star formation histories are available for a large number of dwarf galaxies, it does not make sense to compare these results with specific models of star formation. Such comparisons will eventually allow us to characterize such quantities as the size, duration, efficiency, and regulatory factors of star forming regions in dwarf galaxies.

## 7. Summary

We have measured stellar photometry from deep Cycle 7, F555W and F814W, WFPC2 images of the dwarf irregular galaxy Sextans A. The photometric measurements are in good agreement with previous, Cycle 5, WFPC2 observations of a different field in this same galaxy. By combining the two data sets, we have nearly complete coverage of the optically visible portion of the galaxy.

The CMD from the new Cycle 7 observations is nearly 2 magnitudes deeper than the Cycle 5 observations. This allows unambiguous separation of the faint BHeB stars from contaminants, such as red clump stars and MS stars.

We calculated the recent global SFH using both the MS and BHeB stars. With the photometric limits achieved, we can use the MS to probe to an age of 200 Myr. This allows us to compare the MS and BHeB calculations and verify the consistency of the model and method. We find excellent agreement between the two calculations, both in form and value. Systematic uncertainties in the distance, IMF, and stellar evolution models still restrict the precision of the SFR value to a factor of 2. However, the relative values, and hence the general pattern of changes in SFR, is much better determined.

The BHeB stars provide a reliable SFR calculation back to 700 Myr. The global SFH from the Cycle 7 data is remarkably identical to that of the Cycle 5 data. This implies that both halves of the galaxy have undergone the same spatially averaged SFH.

We used both the Cycle 5 and Cycle 7 data to examine the spatially resolved star formation history over the past 700 Myr. The Cycle 5 data are somewhat unreliable for times older than 500 Myr because of the lower signal-to-noise ratio of these data. We find the stars frequently formed in localized regions, of order 200 pc in size and 100 Myr in duration. However, these regions are not uniformly distributed. Rather, the regions are found in 3 major zones of the galaxy. One of these zones contains star forming regions as old as 400 Myr, and is currently relatively depleted of gas. A second has star forming regions as old as 200 Myr, and is found on the edge of the highest column density neutral gas structure. The third has a single star forming region which is younger than 20 Myr. This youngest region is on the edge of the second highest column density gas structure.

Our interpretation of this star formation pattern is that the star forming regions are orderly stochastic events. Star formation is induced on the edge of gas structures. The subsequent wind and supernova driven shocks begin to break apart the gas structure, while inducing further star formation in nearby, but not coincident, locations. Thus, the star formation eats its way through the gas like a lit fuse until the gas is either converted into stars, or heated and dispersed into the galaxy. A more detailed and quantitative analysis of the star formation process must await a larger sample of galaxies with spatially resolved star formation histories.

Finally, we note that it remains a mystery what caused the sudden increase in SFR over the past 50 Myr. Such fluctuations may be a natural part of the star formation process, and occur periodically, or these may have been induced. In fact, short-lived fluctuations may be hidden in

the past by limitations in our time resolution.

Support for this work was provided by NASA through grant GO-7496, from the Space Telescope Science Institute, which is operated by Aura, Inc., under NASA contract NAS 3-26555. Partial support from NASA LTSARP grants no. NAGW-3189 and NAG5-9221 and the University of Minnesota is gratefully acknowledged. This research has made use of the NASA/IPAC Extragalactic Database (NED) which is operated by the Jet Propulsion Laboratory, California Institute of Technology, under contract with NASA.

## REFERENCES

- Bertelli G., Bressan A., Chiosi C., Fagotto F., & Nasi E. 1994, *A&AS*, 106, 275
- Dohm-Palmer R.C., Skillman E.D., Gallagher J., Tolstoy E., Mateo M., Dufour R.J., Saha A., Hoessel J., Chiosi C. 1998, *AJ*, 116, 1127
- Dohm-Palmer R.C., Skillman E.D., Saha A., Tolstoy E., Mateo M., Gallagher J., Hoessel J., Chiosi C., Dufour R.J. 1997a, *AJ*, 114, 2514
- Dohm-Palmer R.C., Skillman E.D., Saha A., Tolstoy E., Mateo M., Gallagher J., Hoessel J., Chiosi C., Dufour R.J. 1997b, *AJ*, 114, 2527
- Dolphin A. 2000, *PASP*, 112, 1397
- Elmegreen B.G. & Hunter D.A. 2000, *ApJ*, 540, 814
- Gallagher J.S., Littleton J.E., & Matthews L.D. 1995, *AJ*, 109, 2003
- Giovanelli R. & Haynes M.P. 1988, “Extragalactic Neutral Hydrogen” in *Galactic and Extragalactic Radio Astronomy*, eds. Verschuur G.L. & Kellerman K.I., p. 522
- Harris J., Zaritsky D., & Thompson I. 1997, *AJ*, 114, 1933
- Hodge P., Kennicutt R.C., & Strobil N. 1994, *PASP*, 106, 765
- Holtzman J.A., Burrows C.J., Casertano S., Hester J., Trauger J.T., Watson A.M., & Worthey G. 1995, *PASP*, 107, 1065
- Hunter D.A. 1997, *PASP*, 109, 937
- Hunter D.A., Elmegreen B.G., & Baker A.L. 1998, *ApJ*, 493, 595
- Hunter D. A. & Gallagher J.S. 1992, *ApJ*, 391, L9
- Hunter D.A. & Plummer J.D. 1996, *ApJ*, 462, 732

- Ibata R. A., Gilmore G., & Irwin M. J. 1994, *Nature*, 370, 194
- Isserstedt J. 1984, *A&A*, 131, 347
- Isserstedt J., & Kohl, W. 1984, *A&A*, 139, 115
- Kennicutt R.C. Jr., & Skillman E.D. 2001, *AJ*, 121, 1461
- Klypin A., Kravtsov A. V., Valenzuela O., & Prada F. 1999, *ApJ*, 522, 82
- Kwan J., & Valdes F. 1987, *ApJ*, 315, 92
- Maeder A., & Conti P.S. 1994, *ARA&A*, 32, 227
- Mateo M. 1998, *ARA&A*, 36, 435
- Mighell K.J., & Rich R.M. 1996, *AJ*, 111, 777
- Monet D., Bird A., Canzian B., Dahn C., Guetter H., Harris H., Henden A., Levine S., Luginbuhl C., Monet A.K.B., Rhodes A., Riepe B., Sell S., Stone R., Vrba F., Walker R. 1998, U.S. Naval Observatory Flagstaff Station and Universities Space Research Association
- Moore B., Ghigna S., Governato G., Lake G., Quinn T., Stadel J., & Tozzi P. 1999, *ApJ*, 524, L19
- Payne-Gaposchkin C. 1973, *IAU Coll.*, 17, III, 1
- Pearce F.R., Jenkins A., Frenk C.S., Colberg J.M., White S.D.M, Thomas P.A., Couchman H.M.P., Peacock J.A., & Efstathiou G. 1999, *ApJ*, 521, 99
- Piotto G., Capaccioli M., & Pellegrini C. 1994, *A&A*, 287, 371
- Roberts W.W. 1969, *ApJ*, 158, 23
- Roye E.W. & Hunter D.A. 2000, *AJ*, 119, 1145
- Saha A., Sandage A., Labhardt L., Tammann G.A., Macchetto F.D., & Panagia N. 1996, *ApJ*, 466, 55
- Sakai S., Madore B.F., & Freedman W.L. 1996, *ApJ*, 461, 713
- Salpeter E.E. 1955, *ApJ*, 121, 161
- Schaller G., Schaerer D., Meynet G., & Maeder A. 1992, *A&AS*, 96, 269
- Schechter P.L., Mateo M.L., & Saha A. 1993, *PASP*, 105, 1342
- Schlegel D., Finkbeiner D., & Davis M. *ApJ*, 1998, 500, 525
- Searle L., & Sargent W.L.W., 1972, *ApJ*, 173, 25

- Searle L., Sargent W.L.W., & Bagnuolo, W.G. 1973, ApJ, 179, 427
- Skillman E.D. 2000,
- Skillman E. D., Kennicutt R. C., & Hodge P. W. 1989, ApJ, 347, 875
- Skillman E.D., Terlevich R., Teuben P.J., & van Woerden H. 1988, A&A, 198, 33
- Smecker-Hane T.A., Stetson P.B., Hesser J.E., & Lehnert M.D. 1994, AJ, 108, 507
- Steinmetz M. & Navarro J.F. 1999, ApJ, 513, 555
- Tolstoy E. 1999, Ap&SS, 265, 199
- Tolstoy E., Gallagher J.S., Cole A.A., Hoessel J.G., Saha A., Dohm-Palmer R., Skillman E., Mateo M., & Hurley-Keller D. 1998, AJ, 116, 1244
- van den Bergh, S. 2000, The Galaxies of the Local Group, Cambridge University Press
- van Dyk S.D., Puche D., & Wong T. 1998, AJ, 116, 2362
- van Zee L. 2001, AJ, 119, 2757
- van Zee L. 2001, AJ, 121, 2003
- van Zee L., Haynes M.P., Salzer J.J., & Broeils A.H. 1997, AJ, 113, 1618
- Whitmore B., Heyer I., & Casertano S. 1999, PASP, 111, 1559
- Zaritsky D., 1999, AJ, 118, 2824
- Zaritsky D., Harris J., & Thompson I. 1997, AJ, 114, 1002

---

This preprint was prepared with the AAS L<sup>A</sup>T<sub>E</sub>X macros v5.0.

Table 1. Sextans A Cycle 7 WFPC2 Observation Summary

	F555W	F814W	F656N
Orbits	8	16	1
Total Exposure Time (sec)	19200	38400	2400

Note. — Listed are the number of orbits obtained in each filter. Each orbit consists of two exposures, each 1200 seconds long.

Table 2. DoPHOT PSF Shape Parameters

Filter	Chip	FWHM	$\beta_4$	$\beta_6$	$\beta_8$
I	1(PC)	2.6	7.6	-8.3	3.9
	2	1.9	3.6	-1.1	0.4
	3	2.1	3.6	-1.1	0.4
	4	2.0	3.6	-1.1	0.4
V	1(PC)	2.0	7.6	-8.3	3.9
	2	1.7	3.6	-1.1	0.4
	3	1.9	3.6	-1.1	0.4
	4	1.8	3.6	-1.1	0.4

Table 3. Aperture Correction

Filter	Chip	$a(10^{-7})$	$b(10^{-4})$	$c(10^{-4})$	$d(10^{-7})$	$e(10^{-7})$	$f(10^{-7})$	Central Value	Stars	RMS
I	1(PC)	-12.6	-0.21	-4.75	-1.44	3.21	2.38	-0.132	323	0.149
	2	-7.55	-1.68	-1.18	0.73	2.77	0.52	-0.050	1250	0.073
	3	-4.39	-2.50	0.55	1.00	3.62	-2.14	-0.039	969	0.078
	4	-5.71	-2.11	-0.14	0.50	3.60	-1.62	-0.050	1281	0.078
V	1(PC)	-16.3	-2.30	-4.36	3.40	-0.83	5.40	-0.139	254	0.152
	2	-9.59	-0.97	-2.97	-0.29	2.21	3.00	-0.079	787	0.074
	3	-4.20	-2.21	0.44	0.33	3.60	-2.08	-0.041	725	0.069
	4	-7.38	-2.21	-0.86	0.32	5.19	-1.64	-0.061	1170	0.080

Note. — Correction (mag) =  $a + b \times x + c \times y + d \times x^2 + e \times x \times y + f \times y^2$

Fig. 1.— The WFPC2 observations of Sextans A overlaid on a ground-based image taken by Hunter on the 0.9m at CTIO. North is up and east to the Left. The northwestern HST image is from the new observations described in this paper, while the southeastern image is described in Dohm-Palmer et al. (1997a). The HST images were created by combining the F555W (*V*) and F814W (*I*) images. The new observations also include a F656N ( $H\alpha$ ) image, which is shown in red.

Fig. 2.— The internal DoPHOT error distribution for all 39781 stars detected in both the F555W (*V*) and F814W (*I*) filters. The photometric limit is deeper than the Cycle 5 data by 1.5 mag in *V* and 1.8 mag in *I*. The distribution is typical of photometric measurements. The scatter above the main locus is due to stellar image crowding.

Fig. 3.— The completeness fraction based on artificial star tests. The solid line represents the fraction of stars recovered in *V*, while the dashed line represents the fraction of stars recovered in *I*. The error bars indicate Poisson errors based on the number of input artificial stars. Notice that the fraction of recovered star for magnitudes between 22 and 26 lies between 80% and 90%. This is an effect of stellar image crowding. The photometric fidelity of the artificial stars was excellent.



Fig. 4.— The color-magnitude diagrams for Sextans A. The left panel shows the Cycle 5 data, and the right panel shows the Cycle 7 data. The right axis shows the absolute magnitude for the adopted distance modulus of  $(M - m) = 25.8$ . The data have been corrected for Galactic extinction. The most obvious difference between the two data sets is the increased photometric sensitivity of the Cycle 7 data. The curves come from the stellar evolution models of Bertelli et al. (1994), and indicate the main sequence, the blue edge of the He-burning loop, and the red edge of the He-burning loop. The polygonal regions indicate the selection regions for the MS, BHeB, and RGB. Brighter than  $V = 22$  the color index of the blue and red supergiants differ from the models. However, for fainter stars the agreement between the model curves and the data is excellent, particularly for the faint BHeB sequence.

Fig. 5.— The main sequence luminosity function. The Cycle 7 data are shown with a solid line and the Cycle 5 data are shown with a dotted line. The data have been corrected for extinction, and completeness. The bins are 0.3 magnitudes wide. The errors indicate both Poisson errors and completeness errors. Near the top of the plot are indicated the turnoff ages for several values. There are some subtle changes in slope near  $V = 22$  and  $V = 24$ , otherwise the histogram is featureless. The Cycle 5 data does not extend as faint as the Cycle 7 data, but otherwise the two are very similar.

Fig. 6.— The star formation history based on the main sequence. The data have been corrected for reddening and incompleteness. The bin widths are 0.3 magnitudes in  $V$ , and, hence, vary in width with age. Error bars include Poisson errors and completeness correction errors. The left panel shows the calculation using the Padua stellar isochrones (Bertelli et al. 1994) to normalize the histogram. The right panel shows the calculation using the Geneva stellar evolution models (Schaller et al. 1992). Also for comparison, the star formation history based on the BHeB stars has been plotted as a dotted line in both panels using the respective models. The main feature of the Padua solution is a strong rise in SFR near 25 Myr, which is shown in both the MS and BHeB calculations. For ages greater than 75 Myr, the BHeB calculation is consistently lower by about a factor of roughly two. The Geneva models predict a slightly lower mass and turnoff age for a given magnitude. Thus, we see the peak lowered in value and shifted to roughly 50 Myr. However, for ages older than 75 Myr, the Geneva model shows slightly better agreement with the BHeB calculation. Finally, notice that the BHeB SFH using the Padua models agrees in both age and value very well with the BHeB SFH using the Geneva models.

Fig. 7.— The luminosity function of the blue He-burning supergiants from the Cycle 7 observations. Near the top the age is indicated for several magnitude values. The data have been corrected for Galactic extinction and incompleteness. The bins are 0.3 magnitudes. The error bars contain both Poisson errors and errors from the incompleteness correction. For comparison, the Cycle 5 data has been plotted with a dotted line. There is a plateau between  $V = 21$  and  $V = 22.5$  indicating a reduction in the SFR.

Fig. 8.— The global star formation history of Sextans A over the past 700 Myr. The calculation based on the Cycle 7 data is shown with a solid line. For comparison, the calculation based on the Cycle 5 data is shown with a dotted line. The calculations used the  $Z = 0.001$  stellar evolution models of Bertelli et al. (1994), and a power law IMF with a Salpeter (1955) slope ( $-1.35$ ). The bins are 0.3 mag wide in  $V$ , and hence vary in width with age. As was true in Fig. 6 the main feature is an increase in SFR at the youngest times. The Cycle 5 and Cycle 7 calculations are nearly identical, indicating that both halves of the galaxy have undergone the same average history, despite the details of the star formation events being different. The apparent enhancement of SFR in the Cycle 5 data over the Cycle 7 data for oldest times, is due to contamination of the BHeB population from other populations, such as the red clump.

Fig. 9.— This figure is identical to the HST insets of Fig. 1 except they have been rotated counter-clockwise such that the edges are nearly parallel with the axes. The Cycle 5 image is in the lower left with the PC towards the upper right. The Cycle 7 image is in the upper right, rotated nearly 180 degrees compared to the Cycle 5 image. Where the two images overlap, the Cycle 7 image is shown.

Fig. 10.— The stellar density maps for the MS and BHeB stars. The top row is the MS density and the bottom row is the BHeB density. The data have been divided into 4 different age groups: 20 – 50 Myr, 50-100 Myr, 100-150 Myr, and 150-200 Myr. The density is shown in both color (ranging from 0 to 3500 stars  $\text{kpc}^{-2}$  for the MS and 0 to 100 stars  $\text{kpc}^{-2}$  for the BHeB) and contours (with levels of 500, 1000, 1500, 2000, 2500, 3000, and 3500 stars  $\text{kpc}^{-2}$  for the MS, and 25, 50, 75 and 100 stars  $\text{kpc}^{-2}$  for the BHeB). The maps were convolved with a Gaussian with  $\sigma = 80$  pc. For reference, one star per convolution beam is 25 stars  $\text{kpc}^{-2}$ . Because of photometric depth limitations, the Cycle 5 portion of the maps (lower left) do not extend beyond 100 Myr. Both the MS and BHeB stars are primarily found in discrete, concentrated regions, indicating both recent and past star formation sites. In the BHeB maps, notice how the star forming regions can appear in one frame but disappear from the next. This indicates the duration of these star forming regions is of order 50 Myr or less. This is not as apparent in the MS maps because selecting by age only allows us to isolate stars *younger* than the turnoff age. Hence the older MS maps also contain stars whose ages correspond to the younger maps.

Fig. 11.— The stellar density map of the RGB stars. The density is shown in both grey-scale (ranging from 1400 to 3000 stars  $\text{kpc}^{-2}$ ) and contours (with levels 1400, 1800, 2200, 2600, and 3000 stars  $\text{kpc}^{-2}$ ). The map was convolved with a Gaussian kernel with  $\sigma = 80$  pc to match the resolution of Fig. 10. One star per beam is 25 stars  $\text{kpc}^{-2}$ . The RGB are centrally concentrated in a bar structure, and smoothly distributed throughout the galaxy. The orientation of this bar matches the projected morphological bar determined from HI kinematics in Skillman et al. (1988).

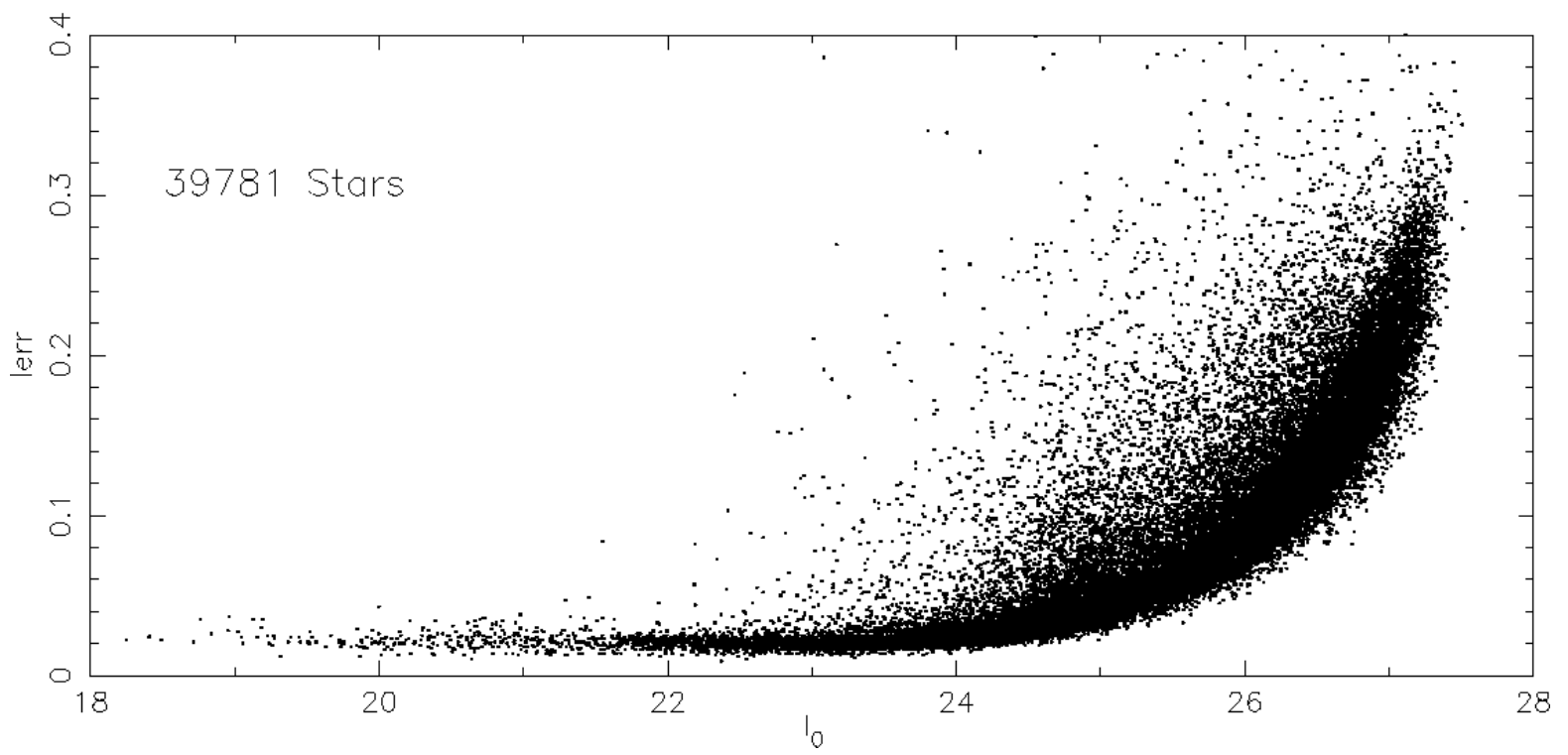
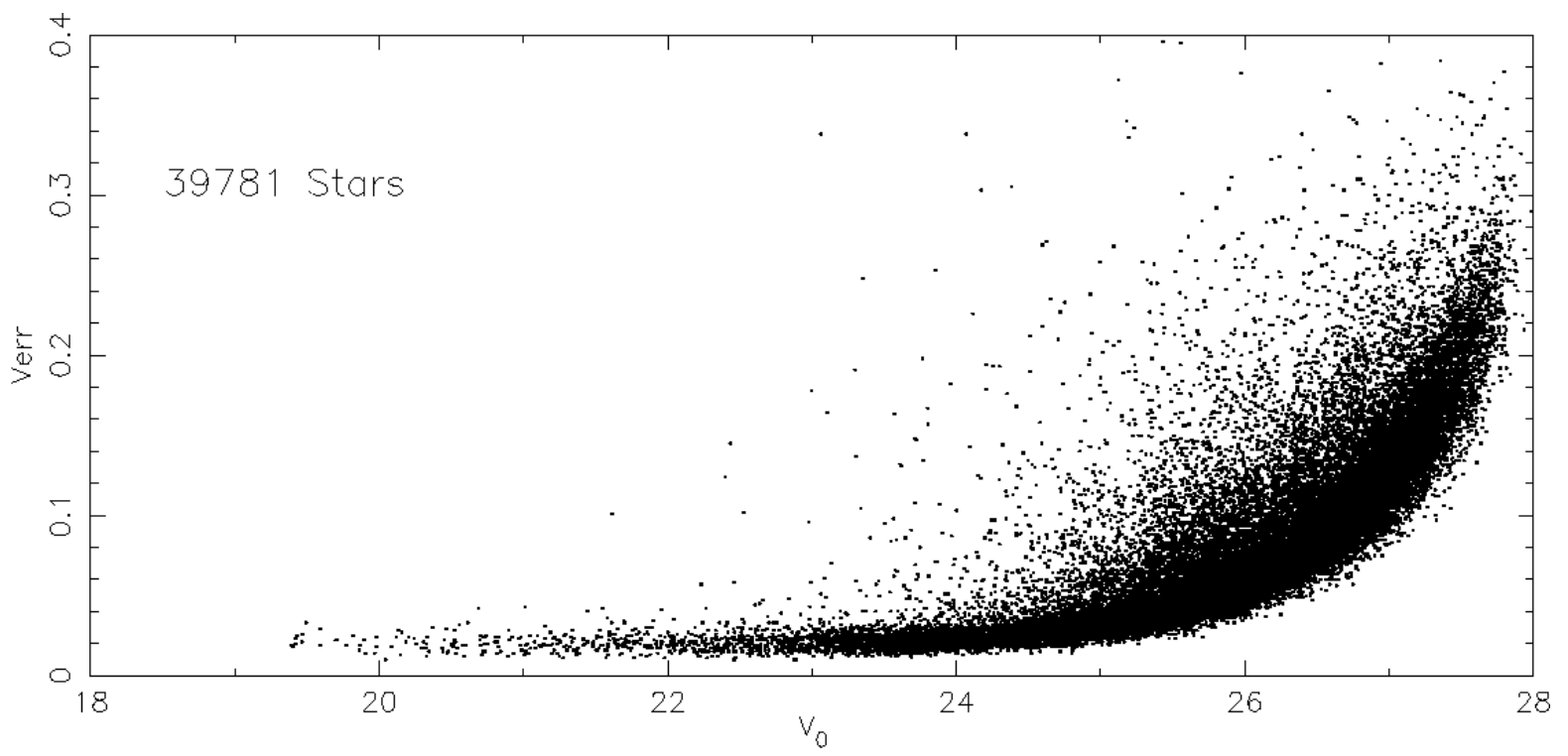
Fig. 12.— The spatially resolved star formation history of Sextans A. The nine panels show selected still frames from the full movie. The movie was convolved with a Gaussian kernel with  $\sigma_{xy} = 80$  pc, and  $\sigma_t = 30$  Myr. The intensity transfer function, and spatial reference is labeled on the central frame. The orientation of the frames is the same as Fig. 9. The SFR ranges from 0 to  $4000 M_{\odot} \text{ Myr}^{-1} \text{ kpc}^{-2}$ . The frames are not uniformly distributed in time, rather they were chosen to highlight peaks and valleys in the SFR. Most of the activity is found on the left side of the maps, and found in two primary zones: upper left and lower right. The lower right zone is associated with the highest column density neutral gas.

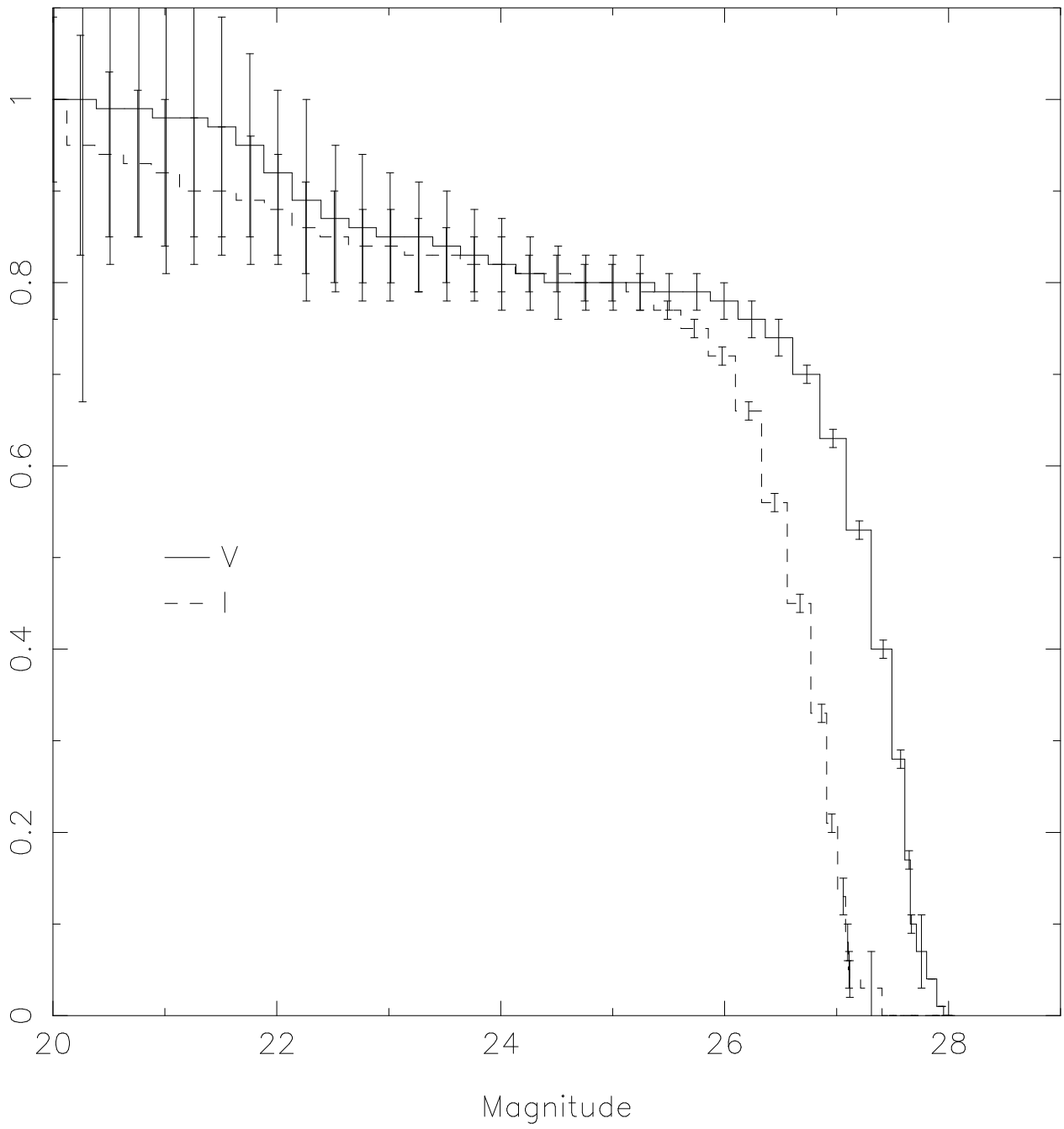
Fig. 13.— The spatially resolved star formation history of Sextans A over the past 100 Myr. The nine panels show still frames from the full movie. The movie was convolved with a Gaussian kernel with  $\sigma_{xy} = 80$  pc and  $\sigma_t = 6$  Myr. The intensity transfer function, and spatial reference is labeled on the central frame. The orientation of the frames is the same as Fig. 9. The SFR ranges from 0 to  $15000 M_{\odot} \text{ Myr}^{-1} \text{ kpc}^{-2}$ . The SFR for these young ages is much higher than it is for the older times (Fig. 12). There is no concentrated star formation in the upper right portion of the maps until the last 20 Myr. This region, which coincides with the second highest neutral gas column density, is clearly the youngest.

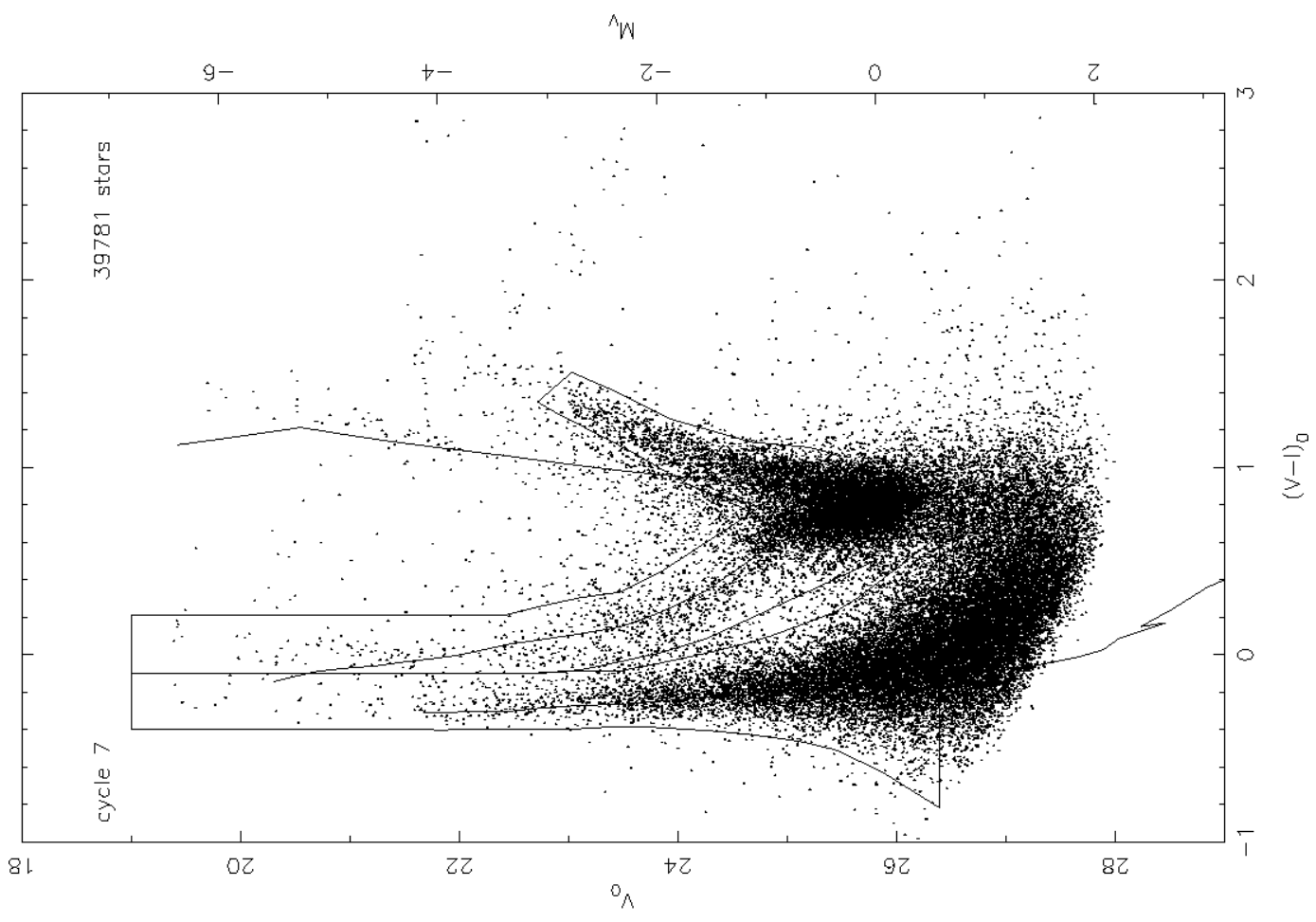
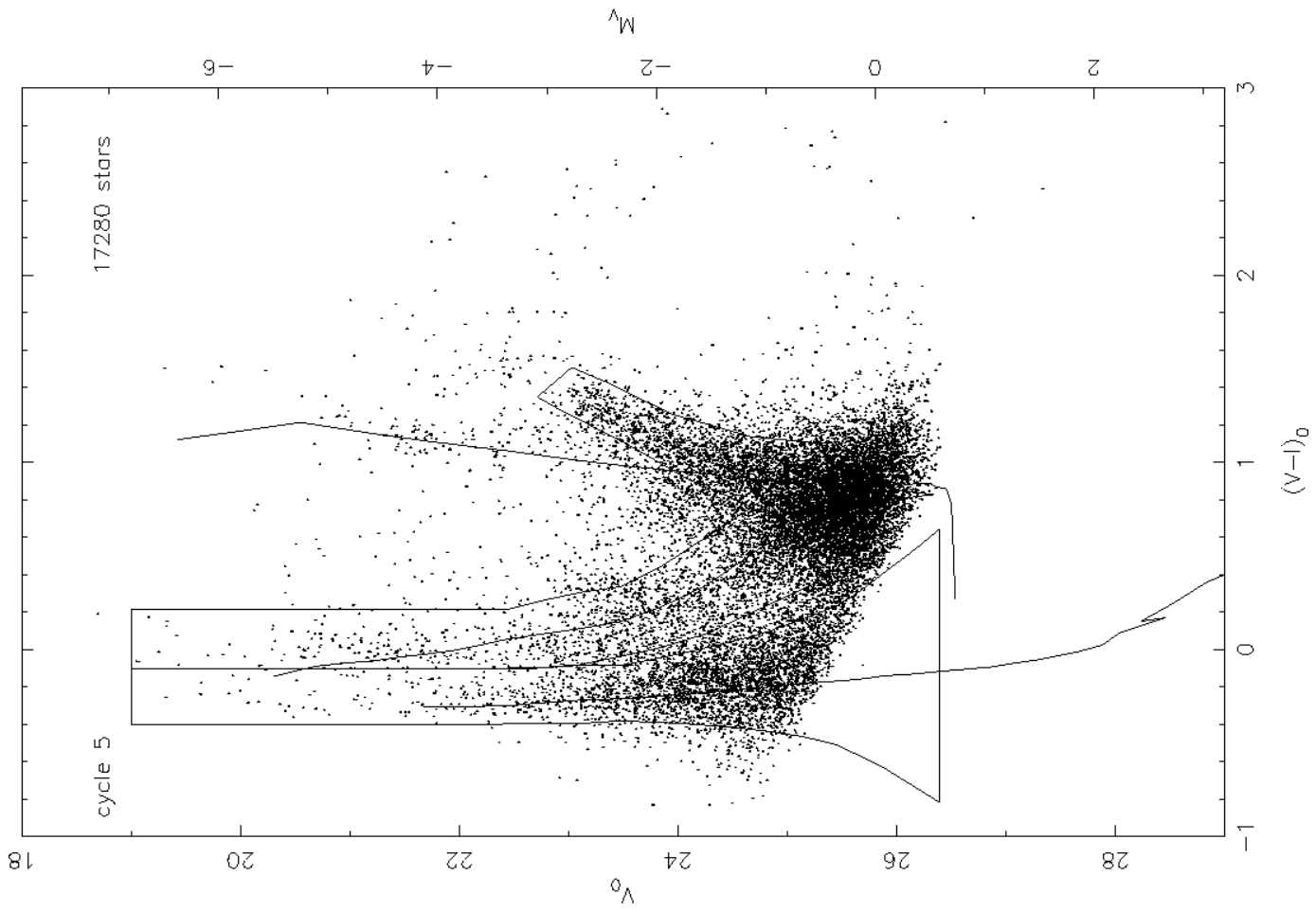
Fig. 14.— The neutral gas column density in both contours over a grey-scale image of the HST data. The units of the HI are  $10^{20} \text{ cm}^{-2}$ . The Cycle 5 field is toward the southeast, and the deeper Cycle 7 field is toward the northwest. The main features are two kidney shaped structures of high column density on opposite sides of the galaxy. These are connected by a lower column density ring, and surround a central depression. However, note that the central region still contains a fairly high column of neutral gas, but is only depressed relative to the surrounding ring. Nearly the entire optical portion of the galaxy lies within the central HI depression.

This figure "Dohm-Palmer.fig01.jpg" is available in "jpg" format from:

<http://arxiv.org/ps/astro-ph/0110257v1>

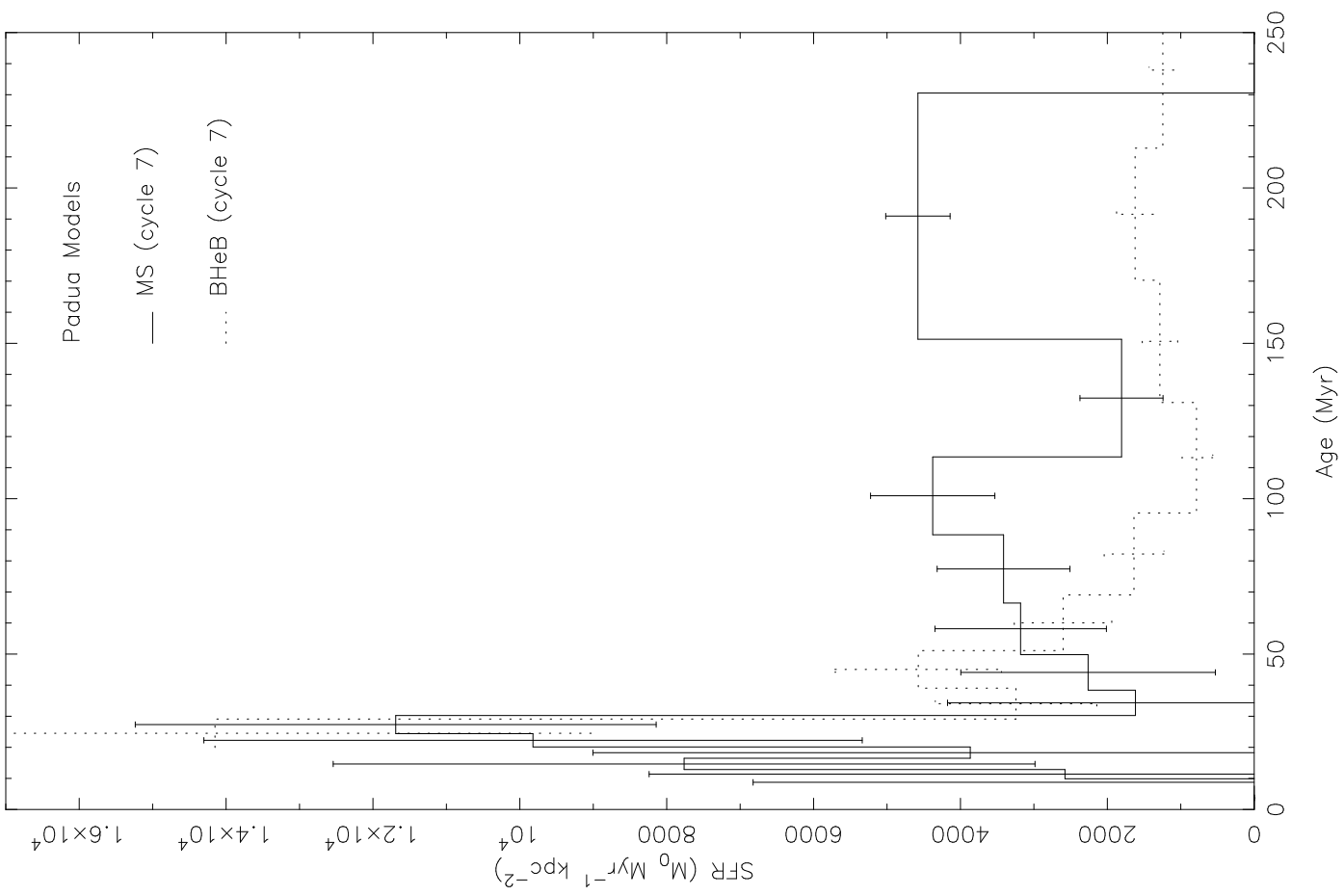
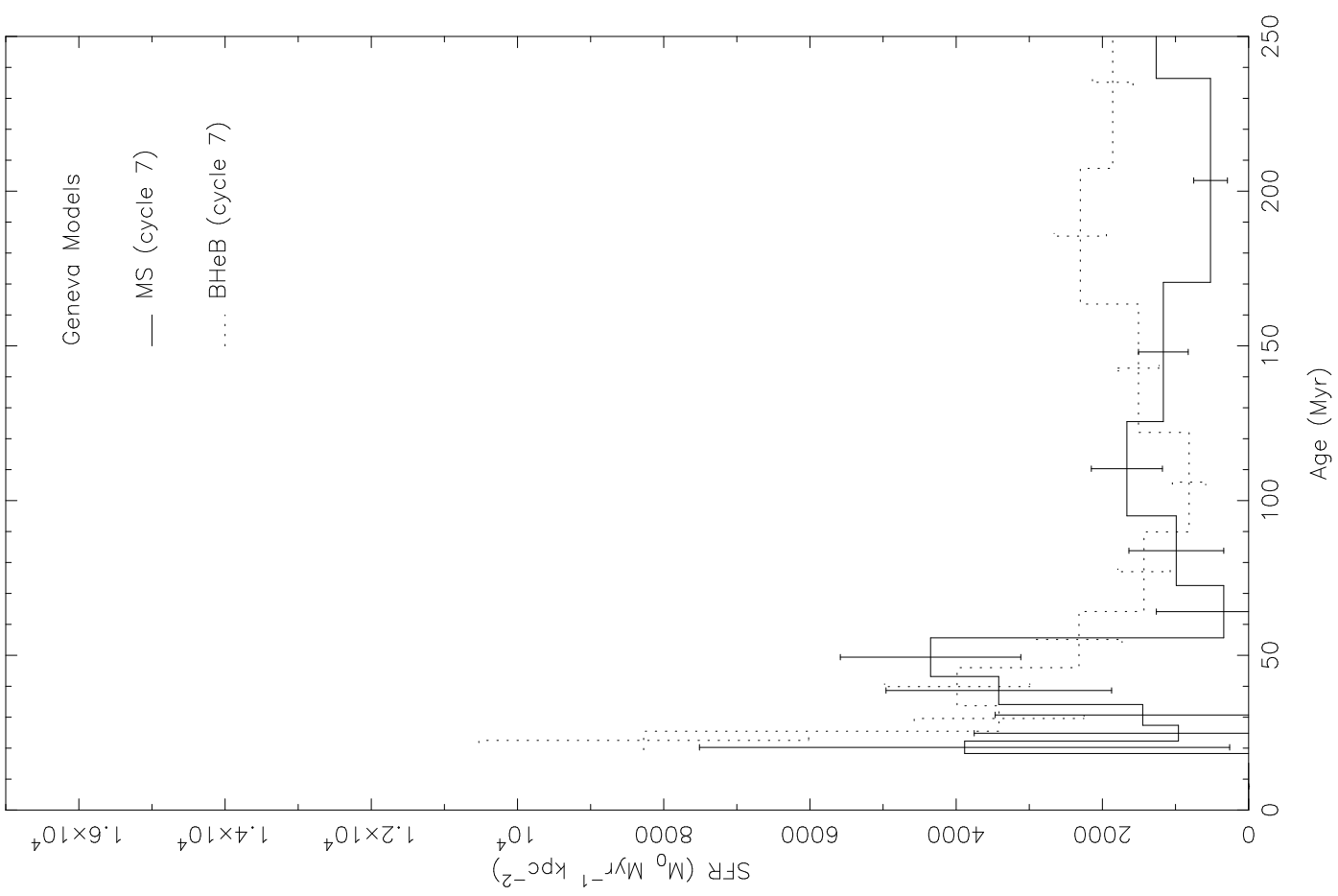


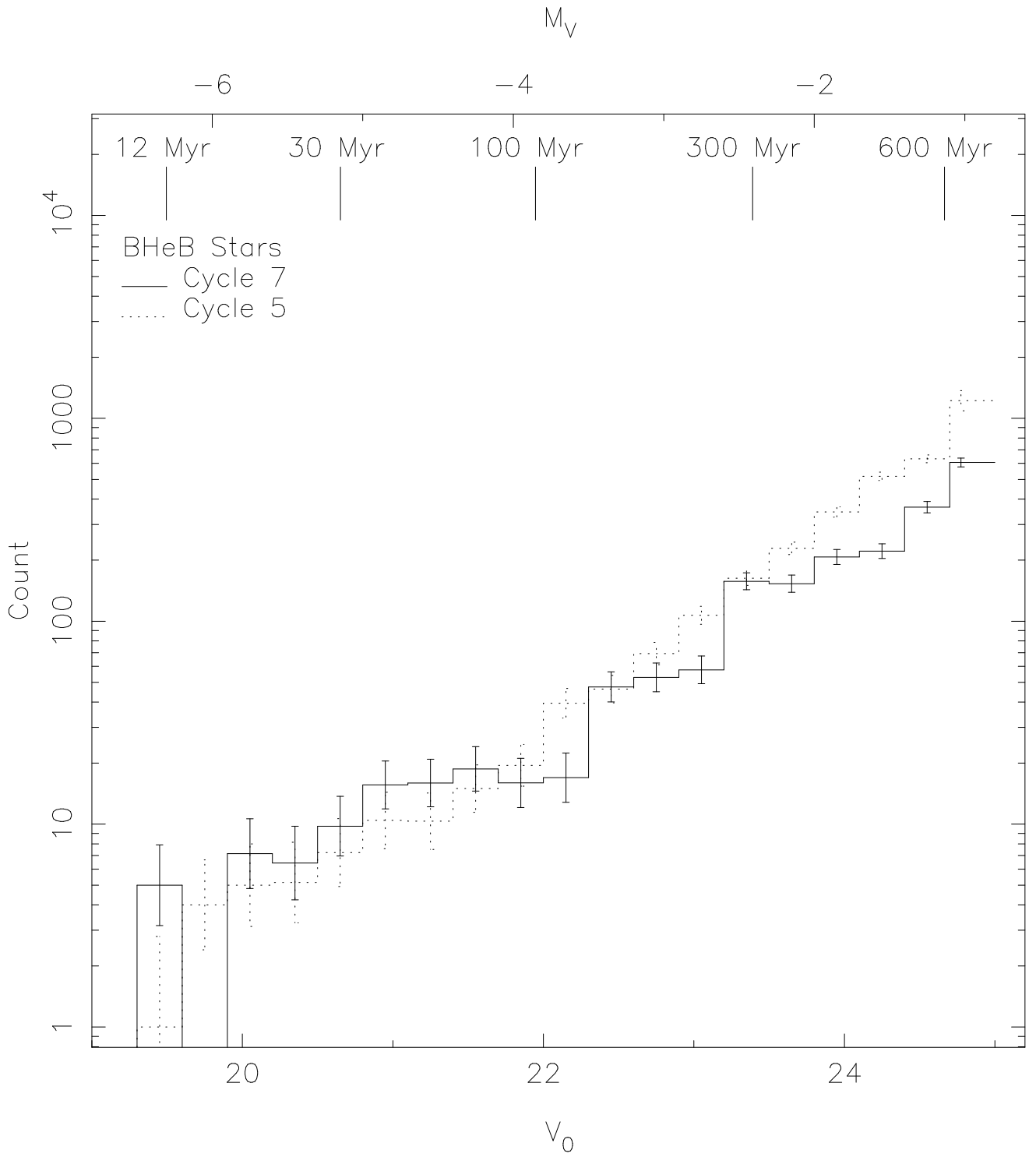


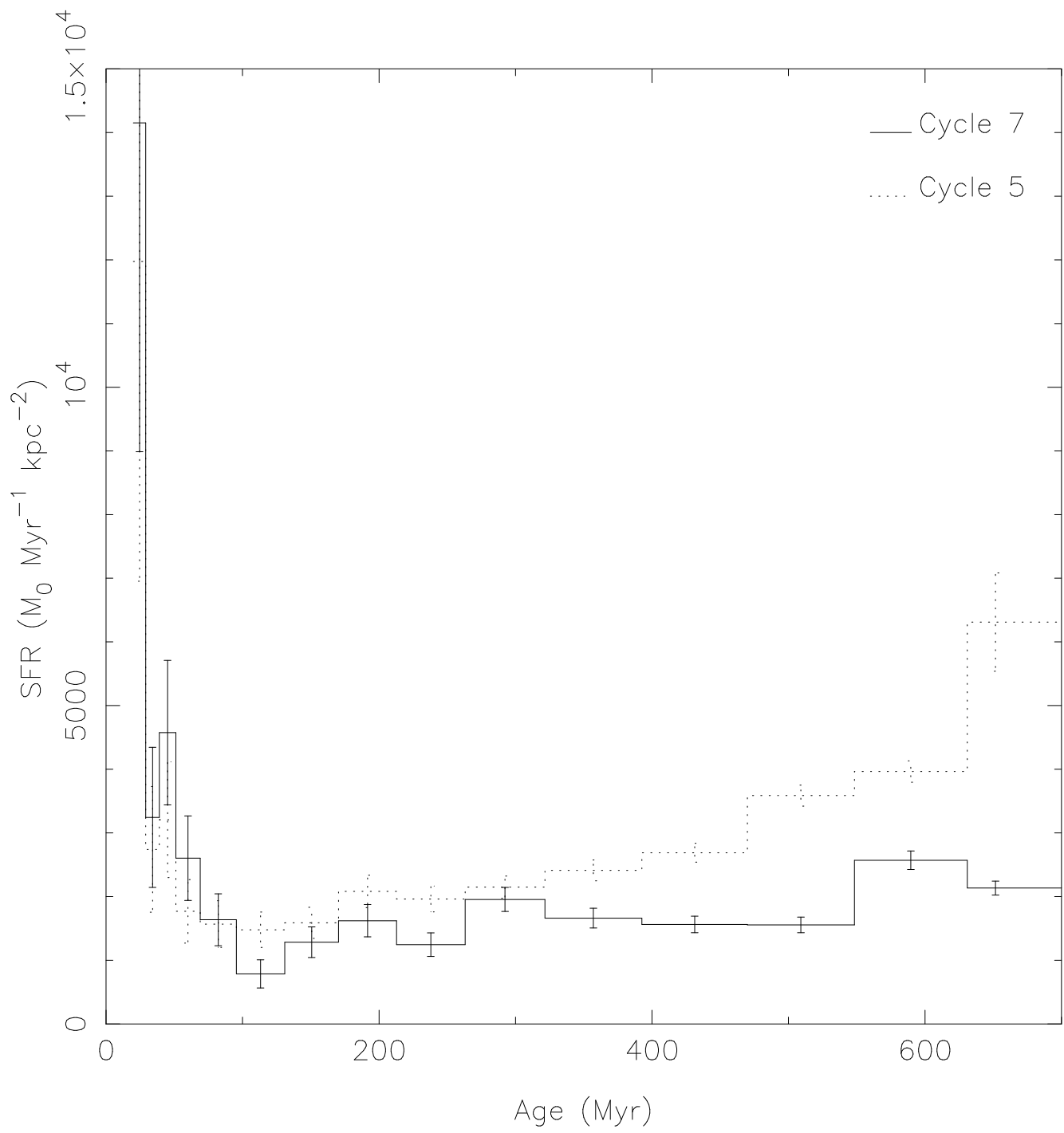










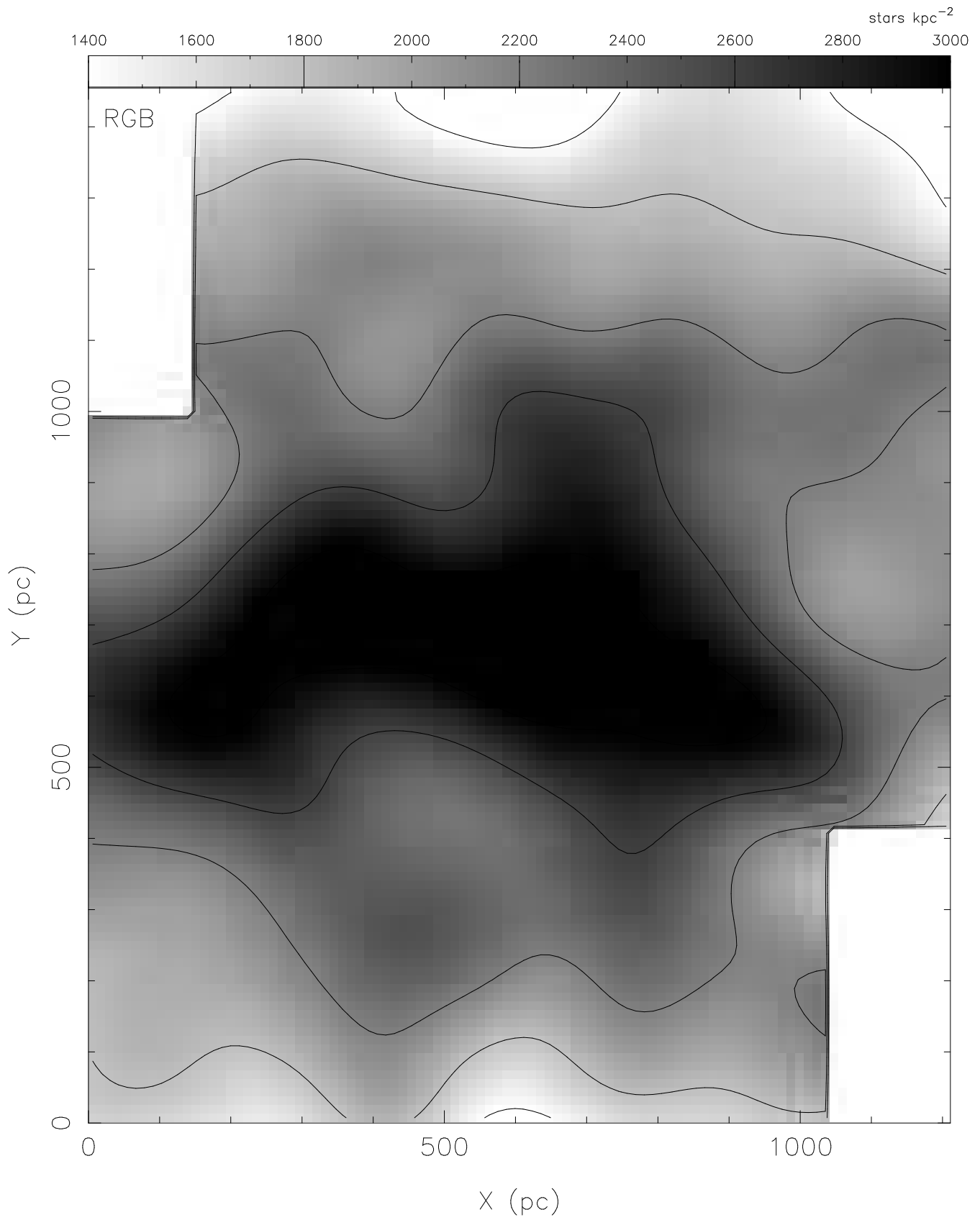


This figure "Dohm-Palmer.fig09.jpg" is available in "jpg" format from:

<http://arxiv.org/ps/astro-ph/0110257v1>

This figure "Dohm-Palmer.fig10.jpg" is available in "jpg" format from:

<http://arxiv.org/ps/astro-ph/0110257v1>



This figure "Dohm-Palmer.fig12.jpg" is available in "jpg" format from:

<http://arxiv.org/ps/astro-ph/0110257v1>

This figure "Dohm-Palmer.fig13.jpg" is available in "jpg" format from:

<http://arxiv.org/ps/astro-ph/0110257v1>

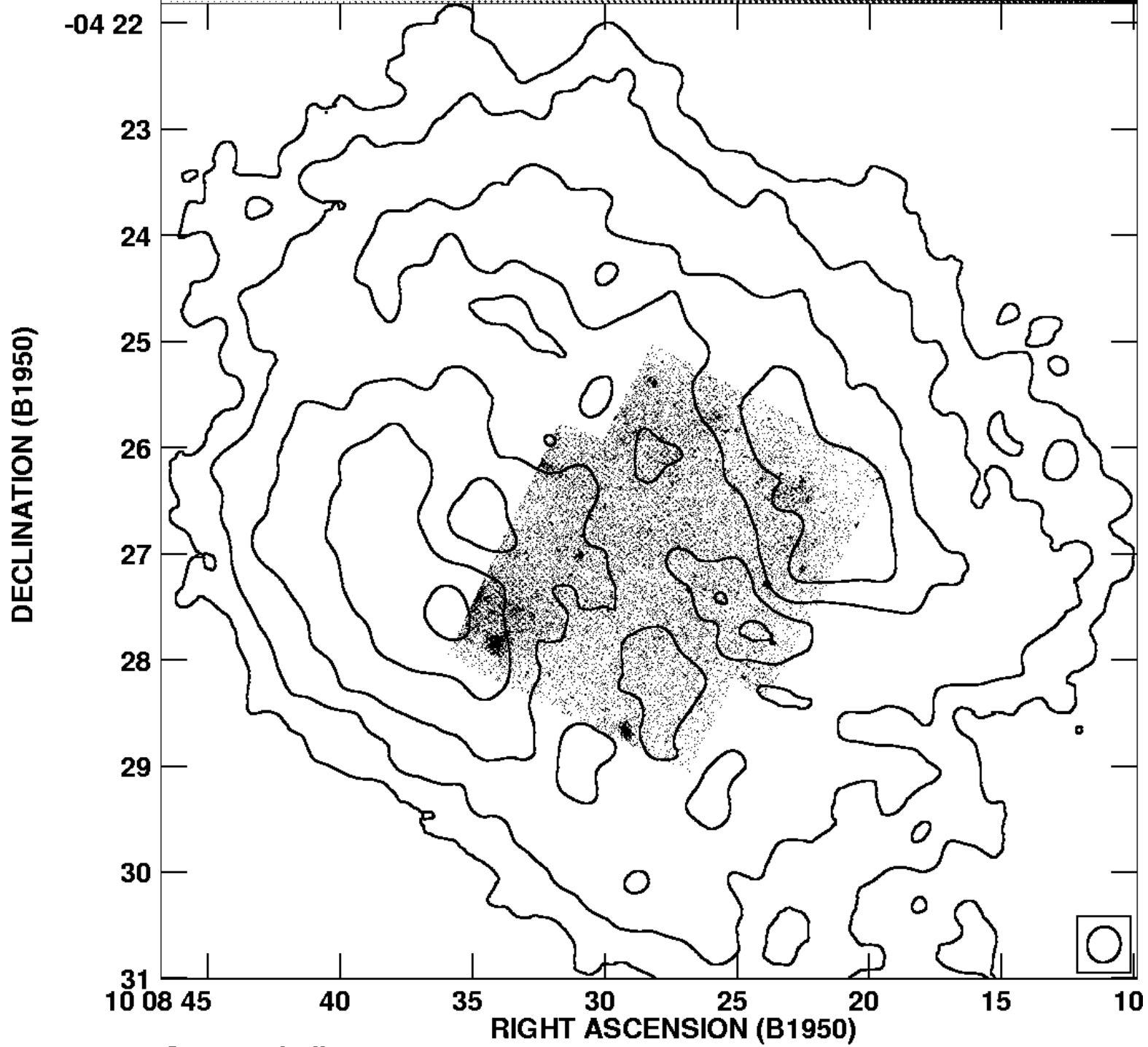


PLot file version 2 created 24-OCT-2000 11:50:42

GREY: V[1/4] SEXA HST.PADIM.1

CONT: SEXTANSA SEXA HI CD B.OHGEO.1

100 110 120 130



Grey scale flux range= 100.0 135.0

Cont peak flux =  $4.8480E+01 \text{ } ^20/\text{CM}^2$

Levs =  $1.000E+00 * (2.500, 5, 10, 20, 40)$